60-m Resolution Soil Moisture Estimation Based on a Multisensor Feedforward Neural Network Model

Gerard Portal, *Member, IEEE*, Mercè Vall-Llossera, *Senior Member, IEEE*, Carlos López-Martínez, *Senior Member, IEEE*, Adriano Camps, *Fellow, IEEE*, Miriam Pablos, *Member, IEEE*, Alberto Alonso-González, *Member, IEEE*, Thomas Jagdhuber, *Senior Member, IEEE*, and Amir Mustofa Irawan, *Member, IEEE*

***Abstract*—Understanding soil moisture (SM) at high spatio-temporal resolution provides crucial insights across various societal disciplines due to its direct impact on environmental and natural disaster monitoring, weather forecasting, agricultural productivity, and water resource management. In recent decades, a variety of algorithms have been developed to improve the spatial resolution of SM maps from passive sensors (∼40 km); however, the resulting maps, often with resolutions around 1 km or even hundreds of meters, still lack the necessary resolution for detailed local analysis. This study addresses this gap by presenting a machine learning methodology aimed at estimating SM at 60-m spatial resolution. A feedforward neural network is employed to capture the relationships among 14 different predictors, including several spectral bands and indices from Sentinel-2, land surface temperature from moderate-resolution spectroradiometer, elevation and slope from shuttle radar topography mission, precipitation from the fifth generation of the European Center for Medium-Range Weather Forecasts Reanalysis for Land, and the sand fraction from SoilGrids250m, with European Space Agency (ESA) Climate Change Initiative (CCI) SM serving as the target variable. The model is trained and applied over the central part of the Iberian Peninsula (38.9 °N–42.5 °N and 3.5 °W–7.2 °W) from 2019 to 2021. At 60-m resolution, the SM maps effectively capture the spatial heterogeneity of the terrain. The temporal analysis demonstrates that high-resolution SM maps preserve virtually the same sensitivity as those from the ESA CCI, with a correlation of 0.66, a bias of 0.095 m^3/m^3, and an unbiased root-mean-square error of 0.044 m^3/m^3 on average.**

***Index Terms*—Climate change initiative (CCI), feedforward neural network (FNN), high-resolution, Sentinel-2, soil moisture (SM), spectral analysis.**

Received 15 May 2024; revised 7 August 2024; accepted 17 August 2024. Date of publication 27 August 2024; date of current version 13 September 2024. This work was supported in part by the Spanish Ministry of Science and Innovation (MCIN/AEI/10.13039/501100011033) through the project INTERACT under Grant PID2020-114623RB-C32 and in part by the Institut d'Estudis Espacials de Catalunya (IEEC) through the NewSpace project. The work of Amir M. Irawan was supported by "La Caixa" Foundation (ID 100010434) through a fellowship under Grant LCF/BQ/DI21/11860028. *(Corresponding author: Gerard Portal.)*

Gerard Portal is with the Institut d'Estudis Espacial de Catalunya, 08034 Barcelona, Spain (e-mail: gerard.portal@upc.edu).

Mercè Vall-Llossera and Carlos López-Martínez are with the Institut d'Estudis Espacial de Catalunya, 08034 Barcelona, Spain, and also with the CommSensLab, Department of Signal Theory and Communications, Universitat Politècnica de Catalunya, 08034 Barcelona, Spain (e-mail: merce.vall-llosera@upc.edu; carlos.lopezmartinez@upc.edu).

Adriano Camps is with the Institut d'Estudis Espacial de Catalunya, 08034 Barcelona, Spain, and with the CommSensLab, Department of Signal Theory and Communications, Universitat Politècnica de Catalunya, 08034 Barcelona, Spain, and also with the UAE University CoE, Al Ain 15551, UAE (e-mail: adriano.jose.camps@upc.edu).

Miriam Pablos, Alberto Alonso-González, and Amir Mustofa Irawan are with the CommSensLab, Department of Signal Theory and Communications, Universitat Politècnica de Catalunya, 08034 Barcelona, Spain (e-mail: miriam.pablos@upc.edu; alberto.alonso-gonzalez@upc.edu; amir.irawan@stmkg.ac.id).

Thomas Jagdhuber is with the German Aerospace Center, Microwaves and Radar Institute, 82234 Wessling, Germany, and also with the Institute of Geography, University of Augsburg, 86159 Augsburg, Germany (e-mail: thomas.jagdhuber@dlr.de).

Digital Object Identifier 10.1109/JSTARS.2024.3450513

I. Introduction

CLIMATE change has been the subject of study for several decades. Arrhenius [1] quantified and analyzed the effect of increasing the concentration of carbon dioxide in the atmosphere and its contribution to the greenhouse effect. Around the 1960s, D. Keeling, motivated by previous studies from S. Arrhenius, began measuring the atmospheric carbon dioxide (CO_2). He observed two trends in the CO_2 variations, the first one with a seasonal oscillation due to the plant growth cycles, and a second one continuing an increasing trend over the time principally due to the effect of human activities (burning of fossil fuels). These two trends were captured in what is known as the "Keeling curve," representing the impact of human beings on the environment and the influence of fossil fuels on climate change [2]. From that period onwards, the consciousness about climate change has been growing ever since. Therefore, scientific research on understanding the impact of its effects on the Earth's ecosystem and human societies is the central task.

In 2010, the international organization Global Climate Observing System defined a group of physical, chemical, and biological variables, known as essential climate variables (ECVs). These ECVs were selected due to their capability of providing crucial information about climatic status, dynamics, and progress for decision-making in the environmental field [3], [4]. Among these ECVs, soil moisture (SM) was tagged as highly relevant, due to its crucial role in linking the Earth's water, carbon, and energy cycles. Moreover, its variation directly impacts the climate, as well as other societal core areas, including water, agriculture, biodiversity, ecosystems, weather, disasters, energy, and health.

European Space Agency (ESA) and the National Aeronautics and Space Administration (NASA) have developed specific missions to estimate SM at a global scale. Within the spectral

© 2024 The Authors. This work is licensed under a Creative Commons Attribution-NonCommercial-NoDerivatives 4.0 License. For more information, see https://creativecommons.org/licenses/by-nc-nd/4.0/

range of microwaves, L-band frequencies are the most suitable to estimate SM at a global scale, including passive and active acquisition techniques [5]. Passive microwave radiometers are characterized by their high radiometric sensitivity (∼0.04 m^3/m^3) and high revisit frequency (∼1–3 days) but low spatial resolution (∼40 km). In contrast, active microwave radars, with their backscatter measurements, provide spatial resolutions that usually range from a few meters to decameters, but in some cases, the temporal resolution can exceed a week. In addition, they are more susceptible to surface geometry influences, such as soil roughness and vegetation structure, compared to passive microwave measurements. At present, two L-band satellite missions are operational for measuring SM: the Soil Moisture and Ocean Salinity (SMOS) [6] and the Soil Moisture Active Passive (SMAP) [7], launched by ESA in 2009 and NASA in 2015, respectively.

The native spatial resolution of the SM maps provided by these missions is suitable for a variety of applications and large-scale studies, such as global climate change monitoring [8], and providing input for early warning systems [9]. However, to meet the needs of local (small-scale) applications, or simply to develop applications requiring finer level of detail regarding the terrain heterogeneity, maps with higher spatial resolution are required. According to a report presented by the United Nations Educational, Scientific and Cultural Organization in 2023 [10], globally, 72% of freshwater withdrawals are done by the agricultural sector. Therefore, these high-resolution SM maps may, for example, assist in achieving more detailed control over water resource management in agriculture on the field level, which is crucial in the current context of climate change, with severe droughts affecting agricultural production hotspots in different parts of the world [11].

Over the last decade, various techniques have been proposed to enhance the resolution of the SM maps provided by satellite missions [12], [13]. There are several ways of classifying these subpixel disaggregation techniques, such as according to the nature of the model used to link the input parameters with the SM, i.e., physically-based [14], [15], semiempirical [16], [17], and data-based models [18], [19]. While physically-based models approximate the processes involved in the dynamics of the SM and may not fully encapsulate the complexity of the system due to model abstraction, data-based models directly learn from data. These machine learning (ML) algorithms allow to capture nonlinear relationships between input variables and SM without relying on predefined assumptions or prior system knowledge. Conversely, ML training requires a large number of high-quality samples representative of the area of interest to enable accurate and effective generalization of the model.

Although the concept of ML has its roots dating back to the 1950s [20], [21], it was not until recent decades that it became widely popular. This surge in popularity can be attributed to several factors: the availability of vast amounts of data, enabling the development of more complex and accurate models; the increase in computational power, particularly the development of graphical processing units, which allow for training of complex models within a reasonable timeframe; and the development of new algorithm and techniques, facilitating efficient model training [22], [23].

In the realm of high-resolution SM estimation, numerous studies have emerged, wherein the core [24], [25], [26], [27] or significant components [28] of the disaggregation process are based on ML techniques to generate SM at scales of a few tens of meters. Chaudhary et al. [24] utilized 12 statistical and ML algorithms for SM estimation, leveraging radar backscatter data from Sentinel-1 and in situ measurements over wheat crops for model training. The study concluded that subtractive clustering exhibits superior performance in terms of bias, Pearson's correlation coefficient (R), and root-mean-square error (RMSE), while also being less computationally expensive than the other methodologies tested. A similar analysis was conducted by Singh and Gaurav [26], but instead of exclusively using Sentinel-1 data, the study also incorporates Sentinel-2 information and Shuttle Radar Topography Mission (SRTM) data to obtain an SM product at a spatial resolution of 60 m and a temporal resolution of six days. Among other ML algorithms, a fully connected feedforward neural network (FNN) resulted in the best performance but also the highest time complexity.

Remote sensing data from autonomous aerial vehicles may offer higher spatio-temporal resolution than sensors onboard satellites. Zhang et al. [27] utilized red-green-blue (RGB), MultiSpectraL (MSL), and Thermal InfraRed (TIR) data acquired by an autonomous aerial vehicle to monitor SM in areas with varying levels of irrigation. Their findings indicated that Random Forest (RF) was the most accurate model among the three proposed for estimating SM. Similarly, Salunke et al. [25] utilized RGB bands acquired from an autonomous aerial vehicle to estimate SM, with eXtreme Gradient Boosting (XGB) emerging as the most accurate algorithm for SM prediction among the three models tested.

ML is also commonly used to downscale the coarse resolution SM maps obtained with satellite sensors, such as those provided by the SMOS, SMAP, or Advanced Microwave Scanning Radiometer for Earth observing system (AMSR-E) missions. In [18], the SMOS SM maps were downscaled using the own information from SMOS, integrated with moderate-resolution imaging spectroradiometer (MODIS) land surface temperature (LST) data, with artificial neural networks (ANN) outperforming other ML algorithms. Im et al. [29] also studied the use of MODIS data, including surface albedo, LST, normalized difference vegetation index (NDVI), enhanced vegetation index (EVI), and evapotranspiration, to disaggregate the AMSR-E data, used as reference by the model, from 25 to 1 km. The RF approach was statistically superior to other ML algorithms. A disaggregation method for SMAP SM was proposed by Xu et al. [30] to achieve a spatial resolution of 1 km from the original 36 km using a wide and deep learning method. SM superresolution (3 m) maps were obtained by Du et al. [19], using several regression-tree methods including RF, gradient boosting regression (GBR), and Light GBR. These models integrated information from SMAP and high-resolution information from Planet SuperDove.

This work proposes a methodology to estimate SM at a spatial resolution of 60 m using an ML model to capture relationships among various predictors. These predictors include Sentienl-2 MSL data (several bands and vegetation/soil indices),

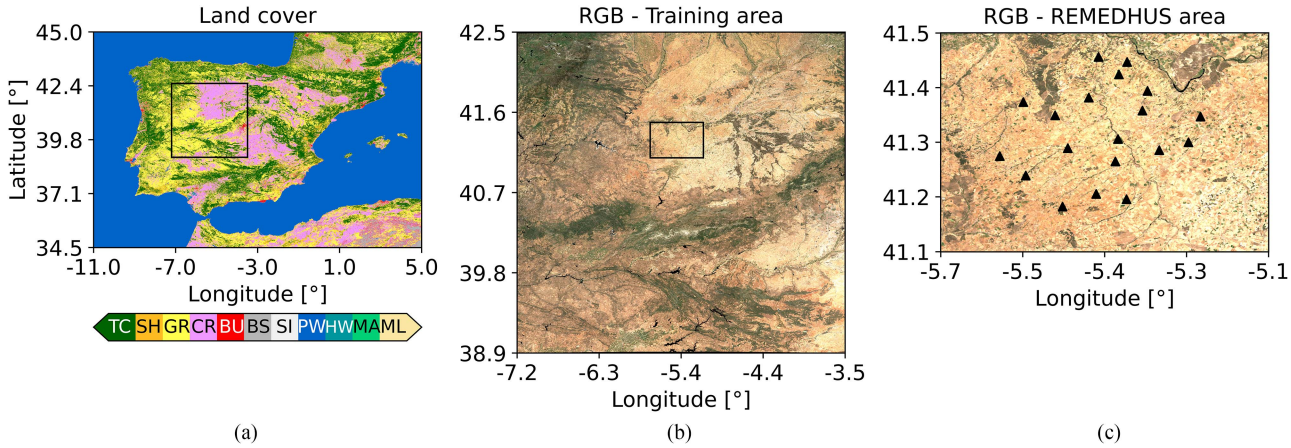

Fig. 1. (a) Land cover map of the Iberian Peninsula, including 11 land cover classes: Tree cover (TC); Shrubland (SH); Grassland (GR); Cropland (CR); Built-up (BU); Bare/sparse vegetation (BS); Snow and Ice (SI); Permanent water bodies (PW); Herbaceous Wetland (HW); Mangrove (MA); and Moss and lichen (ML). The black square in (a) indicates the entire study area, which was used to train the algorithm. (b) Zoom-in view of the training area. The black square in (b) denotes the validation area (REMEDHUS). (c) Zoom-in view of the REMEDHUS area where triangular markers indicate the location of all the in situ SM stations.

MODIS TIR data (LST), SRTM topographic data (elevation and slope), reanalysis information (precipitation) from the fifth generation of the European Center for Medium-Range Weather Forecasts (ECMWF) Re-Analysis for Land (ERA5-Land), and SoilGrids250m soil texture data [sand fraction (SF)], with ESA Climate Change Initiative (CCI) SM as the target variable.

For this study, an FNN with a tabular approach for the datasets has been used. This allows us to handle information gaps in the input data, such as those from Sentinel-2, whose data can be masked by atmospheric effects. While more complex ANN, such as transformers, are effective in constructing sequential images and capturing long-range dependencies [31], and CNNs excel at capturing spatial features [32], their implementation might be limited by spatial and temporal gaps in the input data. In addition, FNNs are relatively straightforward to implement, facilitating reproducibility, and have shown excellent results in high-resolution SM estimation, sometimes outperforming other models [18], [26].

The rest of the article is organized as follows. The study area along with all included variables is presented in Section II. Section III describes the processing applied to the data, how the predictors used by the model are selected, how the model is implemented, and how the results are validated. The study results are shown in Section IV. Section V develops a discussion of the most relevant results, justifying the findings and proposing potential improvements. Finally, Section VI provides the main conclusions.

II. Test Area and Data Description

A. Study Area

The area selected for this study covers the central part of the Iberian Peninsula, spanning latitudinally from 38.9 °N to 42.5 °N, and longitudinally from 3.5 °W to 7.2 °W, which corresponds to an extension of 131 250 km^2. This inner peninsular region (see Fig. 1), located apart from the thermal stability typically found in coastal areas, experiences cold winters and hot summers. Specifically, it is characterized by a continental Mediterranean climate with cold winters in the north, a subhumid continental Mediterranean and mountainous climate in the central part, a warm inland Mediterranean climate in the southwest, and a continental Mediterranean climate with warm summers in the southeast [33]. The study period encompasses three years, from 2019 to 2021. During this period, the annual mean precipitation, within the main land Spain, was below what was measured during the reference period (1981–2010), with a gradual downward trend. In addition, these three years were regarded as extremely warm. The specific values of precipitation (and air temperature) were 628 mm (and 15.9 °C) [34], 606 mm (and 14.7 °C) [35], and 569 mm (and 14.2 °C) [36], for the years 2019, 2020, and 2021, respectively.

B. In Situ Data

The Soil Moisture Measurements Stations Network of the University of Salamanca (REMEDHUS) is an SM network located in the northwest of Spain, between the provinces of Zamora, Valladolid, and Salamanca [37]. This region is predominantly flat and characterized by a continental semiarid Mediterranean climate. The land is primarily used for rain-fed cereal cultivation, although other areas with less representative land uses, such as irrigated crops, fallow areas, vineyards, or forest-pasture, can also be found. REMEDHUS has been operational since 1999 and consists of 19 stations (during the study period from 2019 to 2021), which provide hourly SM measurements at various depth levels, ranging from 0 to 10 cm. In addition, the REMEDHUS area contains four meteorological stations that measure solar radiation, relative humidity, wind speed, precipitation, air temperature, and reference and potential evapotranspiration. REMEDHUS is part of the International Soil Moisture Network [38], from which the information has been accessed. For this study, the SM corresponding to a depth of 5 cm and the daily precipitation data from the weather stations are utilized.

TABLE I
SENTINEL-2 BANDS

Band	Pixel size [m]	Wavelength (S2-A) [nm]	Wavelength (S2-B) [nm]	Description
B1	60	443.9	442.3	Aerosols
B2	10	496.6	492.1	Blue
B3	10	560	559	Green
B4	10	664.5	665	Red
B5	20	703.9	703.8	Red Edge 1
B6	20	740.2	739.1	Red Edge 2
B7	20	782.5	779.7	Red Edge 3
B8	10	835.1	833	NIR
B8A	20	864.8	864	Red Edge 4
B9	60	945	943.2	Water Vapor
B10	60	1373.5	1376.9	SWIR-Cirrus
B11	20	1613.7	1610.4	SWIR 1
B12	20	2202.4	2185.7	SWIR 2

C. Remote Sensing Data

This section outlines the data used in this study, obtained from remote sensing sensors, while also detailing the key characteristics of the space missions that enabled their acquisition.

1) Stand-Alone Products: In the following sections, we detailed the products that are obtained from sensors onboard a single satellite.

a) Sentinel-2: Sentinel-2 mission is a collaborative effort between ESA and the European Commission within the framework of the Copernicus Program [39]. It consists of a constellation of two satellites: Sentinel-2A and Sentinel-2B, which were launched in June 2015 and March 2017, respectively. These satellites are phased 180° in the same sun-synchronous low-Earth orbit, enabling a joint revisit frequency of five days. They observe the Earth's surface at an incidence angle close to nadir ($\pm 10.3°$). The multispectral images acquired by Sentinel-2 encompass 13 bands, ranging from the visible to the short-wave infrared, with resolutions of 10, 20, and 60 m, depending on the band. The high-resolution, multifrequency data provided by Sentinel-2, along with its regular revisit frequency, make it highly relevant for several applications related to vegetation monitoring, detecting changes in the Earth's surface, assessing water quality, and monitoring natural disasters, among others. Clouds and cloud shadows are masked out in Sentinel-2 surface reflectances [40], and then the resulting values are filtered to exclude those lower than 3e-4 or higher than 1.

For this study, Sentinel-2 Level-2A orthorectified atmospherically corrected surface reflectance data are utilized, obtained from the Google Earth Engine online platform [41]. Ten Sentinel-2 bands are considered (see Table I): B2, B3, B4, B5, B6, B7, B8, B8A, B11, and B12. The B1, B9, and B10 bands, mainly used for atmospheric correction, altitude thresholding, and cloud masking, are excluded from the analysis. From the selected bands, ten vegetation and soil indices are computed, including the NDVI [42], Normalized Difference Red Edge Index (NDRE) [43], EVI [42], Green Normalized Difference Vegetation Index (GNDVI) [44], Soil Adjusted Vegetation Index (SAVI) [45], Normalized Difference Moisture Index (NDMI) [46], Moisture Stress Index (MSI) [47], Normalized Burn Ratio Index (NBRI) [48], Bare Soil Index (BSI) [49], and Normalized Difference Water Index (NDWI) [46].

b) MODIS: NASA MODIS is carried onboard Terra and Aqua polar, sun-synchronous, and low-Earth orbiting satellites, launched in December 1999 and May 2002, respectively [50]. MODIS captures images with 36 spectral bands, ranging from the visible to the TIR, at a moderate spatial resolution. It is capable of providing details of the Earth's surface with spatial resolutions of 250 m, 500 m, and 1 km. This spatial resolution, combined with daily global coverage of the Earth's surface, makes MODIS data crucial for various applications, including vegetation, ice, and snow monitoring, forest fire detection, soil temperature analysis, air quality assessment, and cloud detection, among others. For this study, LST data are obtained from Aqua (MYD11A1 version 6.1) at a spatial resolution of 1 km. These data are accessed through the Application for Extracting and Exploring Analysis Ready Samples[51]. LST values equal to or less than 274 K are filtered out to avoid using information from frozen areas or those close to the freezing point.

c) SRTM: The SRTM was jointly conducted by NASA and the National Geospatial-Intelligence Agency with the objective of creating a comprehensive, high-resolution digital topographic database of the Earth's surface [52]. The mission lasted for 11 days, during which the Endeavour completed 176 orbits. The primary instrument used for this mission was the spaceborne imaging radar (SIR), along with an X-band synthetic aperture radar (SAR) known as SIR-C/X-SAR. The SIR-C/X-SAR consisted of an L- and C-band fully polarimetric radar combined with an X-band single-polarization radar, working as transmitter and receiver antennas. An additional receive-only antenna was mounted at the end of a 60-m mast to allow single-pass interferometry tasks. The SRTM mission achieved a coverage of 80% of the Earth, from 56 °S to 60 °N, with a spatial resolution of 30 m for the acquired data. For this study, the SRTM 1 Arc-Second Global [53] elevation data are utilized, which provide worldwide coverage of void-filled data at a spatial resolution 30 m. These data are accessed from the United States Geological Survey EarthExplorer. Subsequently, the slope parameter is derived

from the digital elevation model (DEM) using quantum geographic information systems software.

2) Combined Products: In the following, we detailed the products obtained by merging information acquired from various satellites.

a) CCI SM: The ESA CCI project was initiated in 2010 with the goal of producing yearly updated products for the most relevant components of the climate system, known as ECVs. The objective of this project is to provide the most comprehensive and longest data record possible, currently spanning from 1978 to the present. SM is one of these ECVs, and the ESA distributes this product under the name ESA CCI SM in three harmonized datasets, including: 1) the active product, which is created by merging scatterometer SM products, derived from the advanced scatterometer and Active Microwave Instrument – WindScat instruments; the passive product, created by merging data provided by the SMOS, SMAP, scanning multichannel microwave radiometer, special sensor microwave imager, tropical rainfall measuring mission microwave imager, AMSR-E, WindSat, FengYun (FY)-3B, FY-3C, FY3D, AMSR2, and global precipitation measurement mission instruments; and the combined active/passive product, which includes all the satellite instruments mentioned above [54]. For this study, the combined product is used owing to its greater temporal and spatial coverage, as well as its superior performance during validation using globally distributed in situ stations, in contrast to both passive and active products. This product provides global coverage SM maps with a spatial resolution of 0.25° (corresponding to a resolution of about 25 km for the study area presented in this analysis) and one-day sampling interval. The most restrictive quality flag available within the files are applied to the data, meaning that only data with no detected inconsistencies are used. Furthermore, values above 0.7 are also filtered out to exclude saturated values from the analysis.

b) WorldCover: The WorldCover dataset is a global land cover product with a spatial resolution of 10 m, derived from data obtained by the Sentinel-1 and Sentinel-2 constellations. The product's legend contains 11 land cover classes, namely: "Tree cover," "Shrubland," "Grassland," "Cropland," "Built-up," "Bare/sparse vegetation," "Snow and Ice," "Permanent water bodies," "Herbaceous Wetland," "Mangrove," and "Moss and lichen." The most recent version of WorldCover, representing the year 2021, was released on 28 October 2022, with an overall accuracy of approximately 77% [55]. In this study, the WorldCover product is utilized at its maximum resolution of 10 m to filter out areas classified as build-up, snow and ice, and permanent water bodies.

c) SoilGrids250m: SoilGrids provides global predictions for various soil properties, including organic carbon, bulk density, cation exchange capacity, pH, soil texture fractions, and coarse fragments, at several depth levels (ranging from 0 to 20 cm), as well as predictions for depth to bedrock and the distribution of soil classes [56]. These predictions are based on a diverse set of soil profiles and various soil variables (primarily derived from MODIS land products and SRTM derivatives, among others), which were used to train an ensemble of ML methods. This study specifically considers the SoilGrids250m clay fraction (CF) [57] and SF [58] at 250-m resolution.

d) ERA5-land: ERA5-Land [59] dataset is derived from the ECMWF dataset known as ERA5, which provides estimates of numerous atmospheric, land, and oceanic variables at a spatial resolution of 30 km. However, ERA5-Land specifically focuses on land components, excluding information related to sea ice and ocean available within the ERA5 dataset. It is a global reanalysis dataset that combines a numerical weather prediction model with observational data to generate a complete and consistent representation of the Earth's climate system. ERA5-Land encompasses 53 variables related to the water and energy cycles over land, providing global coverage at a spatial resolution of 9 km. The dataset offers hourly information from 1981 to the present. For this study, the ERA5-Land total precipitation is used. Hourly maps are used to compute the accumulated precipitation for 3 and 15 days by calculating the sum from the corresponding day backward.

Relevant information regarding all data products used in this study is summarized in Table II.

III. Methodology

This section describes the data processing applied, how the predictors used by the model are selected, how the model is implemented, and how the results are validated. The initial data processing includes filtering and mapping the data to a reference grid. The variable selection process facilitates the exclusion of less pertinent variables. Then, the ML model and target variable used are specified, along with the procedure followed to train the model and estimate the SM at high resolution. Finally, the resulting SM maps are validated at both high and low resolutions, spatially and temporally.

A. Data Processing

The most constrained variable in terms of temporal and spatial coverage is the Sentinel-2 data. Sentinel-2 provides observations with a revisit time of five days, accounting for both Sentinel-2A and Sentinel-2B. Although it provides global coverage, the presence of clouds and other atmospheric effects limit the availability of ground information data. Therefore, all the predictors are resampled to match the 60-m grid resolution of Sentinel-2 using nearest-neighbor interpolation [60]. Then, any areas without Sentinel-2 data are filtered out from all the features. In addition, the WorldCover map [55] is utilized to exclude water bodies, built-up areas, as well as snow and ice regions.

After the data filtering, the variables are prepared for aggregation to the required resolution, ensuring that this procedure is carried out using the same number of samples for all features. The aggregation process involved calculating the average value of all pixels in the source grid that corresponds to the same pixel in the low-resolution (0.25°) target grid. Only high-resolution pixel aggregations, conducted with a minimum coverage of 70% relative to the low-resolution pixel of the target grid, are considered.

Fig. 2 illustrates an example of the filtering and aggregation procedure applied to the CF map, which is initially at a 250 m

TABLE II
SUMMARY OF ALL THE VARIABLES CONSIDERED IN THE STUDY

Source	Variable	Grid	Revisit
In situ			
REMEDHUS	SM and precipitation	In situ	hourly
Stand-alone products			
Sentinel-2	Reflectances, vegetation, and soil indices	60 m	5 days
MODIS	LST	1 km	daily
SRTM	DEM, slope	60 m	static
Combined products			
WorldCover	ESA Land cover	10 m	static
ERA5-Land	Precipitation	9 km	daily
SoilGrids250m	CF and SF	250 m	static
ESA CCI	SM	0.25°	daily

The "Grid" column available in this table represents the grid resolution at which the data have been downloaded. Some data may exist at higher resolutions, such as certain bands of Sentinel-2 or data derived from SRTM.

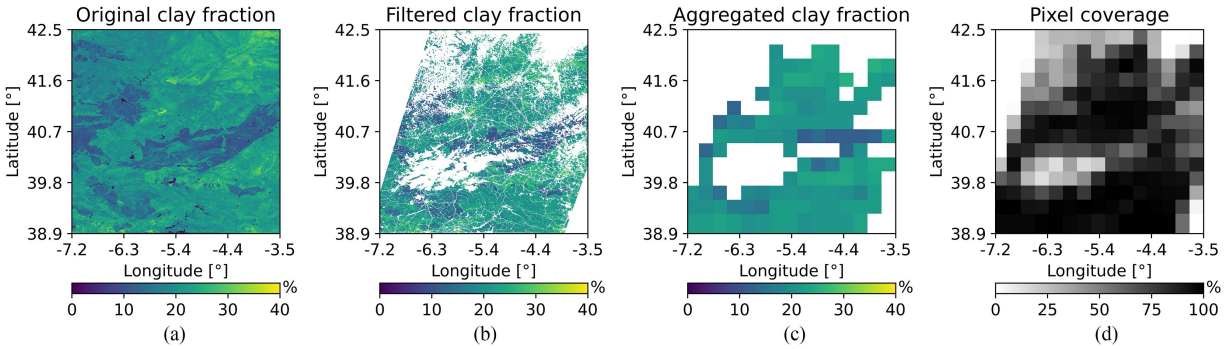

Fig. 2. (a) Native CF map at 250-m resolution. (b) Interpolated and filtered CF map at 60-m resolution. (c) Aggregated CF map at a 0.25° grid. (d) Pixel coverage map.

resolution [see Fig. 2(a)]. It is subsequently interpolated and filtered to a 60-m resolution [see Fig. 2(b)] and finally aggregated to 0.25° [see Fig. 2(c)] but considering only pixels with high coverage [see Fig. 2(d)].

This study utilizes multiple variables characterized by diverse dynamic ranges. To ensure a homogeneous dynamic range across all variables, their distributions are standardized to attain a mean of zero and a standard deviation (std) of one. This standardization is applied using the Z-score methodology, which entails subtracting the dataset's mean and dividing it by the std [61]

$$\boldsymbol{z} = \frac{\boldsymbol{x} - \bar{\boldsymbol{x}}}{\sqrt{\frac{1}{n}\sum_{i=1}^{n}\left(x_i - \bar{\boldsymbol{x}}\right)^2}} \tag{1}$$

where x_i is the ith element of the vector $\boldsymbol{x}$, $\bar{\boldsymbol{x}}$ is the mean of the vector, and n is the total number of samples in the vector.

B. Feature Selection

The variables selected as potential predictors in the FNN model include 3- and 15-days accumulated precipitation from ERA5-Land, sand, and CFs from SoilGrids250m, DEM, and slope from SRTM, MODIS LST, and various Sentinel-2 bands (B2, B3, B4, B5, B6, B7, B8, B8A, B11, and B12), along with specific spectral indices (NDVI, NDRE, EVI, GNDVI, SAVI, NDMI, MSI, NBRI, BSI, NDWI). Only variables that significantly improve the model without introducing excessive redundancy are considered.

Both 3-days and 15-days accumulated precipitation products are included due to their low correlation ($R \leq 0.4$) with all the other variables. Although the CF and SF exhibit a low correlation ($R \leq 0.4$) with the others, they are nearly complementary to each other. Therefore, only the SF is included. DEM and slope show a relatively low correlation ($R \leq 0.5$) with the other products, warranting their inclusion. The MODIS LST, with an $R \leq 0.6$ with other variables, is also included.

Regarding Sentinel-2 bands and indices, some exhibit high correlations with each other. The following methodology has been used for their selection.

1) Entropy is computed for all Sentinel-2 variables, and the one with the highest entropy is selected for application in the model.
2) For the selection of all subsequent variables, not only the entropy of each individual one is considered but also its correlation with the previously selected features. The one with the highest score is chosen. The score is defined as

$$s_j = h_j \cdot \prod_{m=1}^{M}\left(1 - R_{j,m}\right) \tag{2}$$

where j represents the index of the variable under evaluation and M is the number of variables already selected. $\boldsymbol{h}$ is the

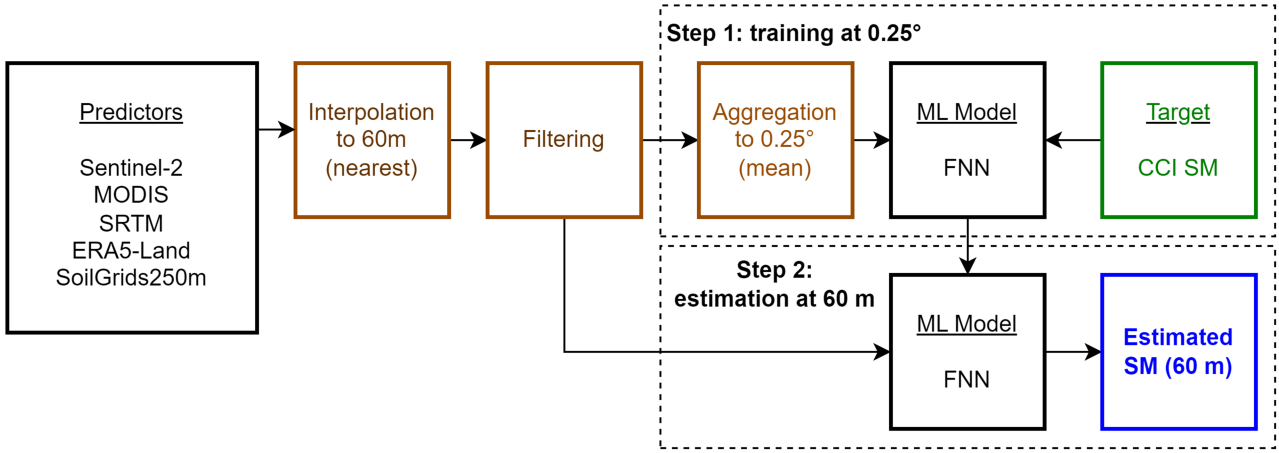

Fig. 3. Flowchart for SM estimation at 60 m. The brown boxes represent the processing applied to the data before being utilized by the model, the green box corresponds to the ESA CCI SM at a resolution of 0.25°, and the blue box corresponds to the resulting SM estimated at 60 m. The two main steps of the disaggregation model consist of: 1) training the model using all variables at a 0.25° resolution, and 2) utilizing the trained model along with the variables on the 60-m grid to estimate the final SM at high resolution.

vector containing the entropies of all the variables, with h_j denoting the jth element of $\boldsymbol{h}$. $\boldsymbol{R}$ is the matrix containing the correlations between all variables, where $R_{j,m}$ denotes the correlation coefficient between the evaluated variable j and the selected variable m. Step two can be repeated as many times as necessary to sequentially select variables.

Following this methodology, the finally selected Sentinel-2 bands are B5, B6, B8A, and B11, while the included spectral indices are NDVI, EVI, GNDVI, and MSI. Taking into account the aforementioned variables included (3-days and 15-days accumulated precipitation, SF, DEM, slope, and LST), the total number of predictors used to build the FNN model is 14. The inclusion of the remaining variables results in only a marginal improvement of 1% in the explained variance, with the RMSE decreasing by 5.5%.

TABLE III
CONFIGURATION OF THE HYPERPARAMETERS USED BY THE ML MODEL

Hyperparameter		Value
Model architecture	**Hidden layers**	2
	Neurons	35 (per hidden layer)
Epochs		800
Learning rate		5e-4
Regularization	**L2**	1e-5
Batch size		32
Activation function		ReLU
Loss function		MSE
Optimizer		Adam

Where RELU refers to rectified linear unit, MSE to mean square error, and Adam to adaptive moment estimation.

C. Model Implementation

An FNN is a type of ANN in which the connections between the neurons do not form cycles but data flow from input to output. It is a supervised learning model, requiring a set of inputs (predictors) and a reference variable (target) for training. The intermediate or hidden layers enable the network to learn complex representations of the data [62]. The method proposed in this study for obtaining high-resolution SM based on FNN networks is summarized as follows (see Fig. 3).

1) Training at 0.25° Resolution: The model is trained using the CCI SM data at a 0.25° resolution as the target variable. To ensure that all the variables are within the same grid, the procedure detailed in Section III-A is applied to filter and aggregate the 14 predictors selected in Section III-B, all aligned to the 0.25° grid of the target variable. A total of 21 354 instances, comprising both training and test data, are fed into the FNN model. The FNN models used in this study are implemented through PyTorch, an open-source deep learning library available in Python [63]. Some of the most relevant hyperparameters are adjusted according to the values presented in Table III. For the analysis of the model performance, the following metrics are calculated: the losses, using the RMSE; the accuracy, which is defined as the number of times per epoch that the difference between the original and the estimated SM is lower than 0.03 m^3/m^3, with the estimated SM within the range $0 \leq \bar{x} \leq 0.7\ m^3/m^3$; and the explained variance. The data are split using the scikit-learn library in Python [64] with the proportion 80/20 (training/testing). To mitigate the impact of the random initialization of weights on the resulting SM maps, five models are trained using the same train/test split. The final SM product is the ensemble of the five models, which helps reduce variability and provides more stable and reliable results.

2) Estimation at 60 m: In this step, all the variables are used at a resolution of 60 m. Certain variables are already at this grid resolution, such as the Sentinel-2 spectral bands and indices, DEM, and slope. However, the rest of the variables undergo a grid transformation using the nearest-neighbor interpolation. These predictors at 60-m grid are fed into the previously trained ML model to estimate the SM at high resolution.

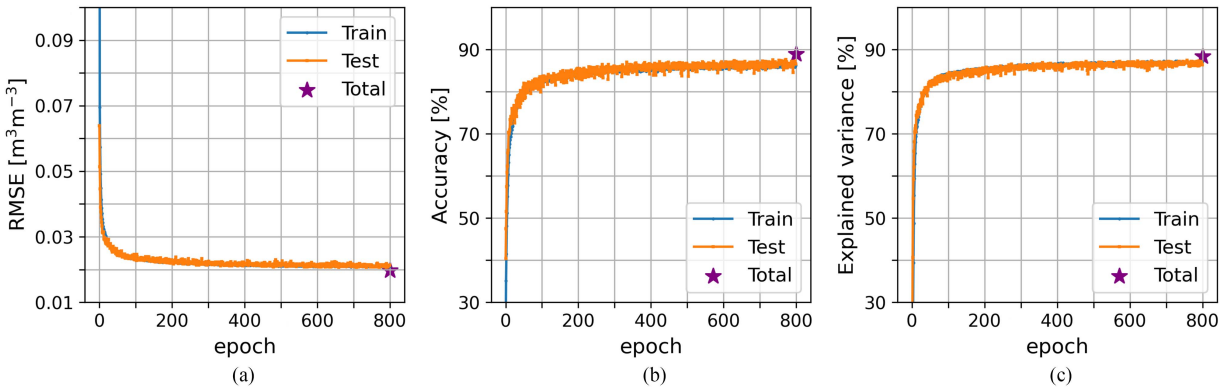

Fig. 4. (a) Losses (or RMSE), (b) accuracy, and (c) explained variance across different epochs for the testing data (blue line) and the training data (orange line). The dark purple marker indicates the final score obtained after passing all data through the pre-trained model: RMSE = 0.02 m^3/m^3, accuracy = 0.89, and R^2= 0.88.

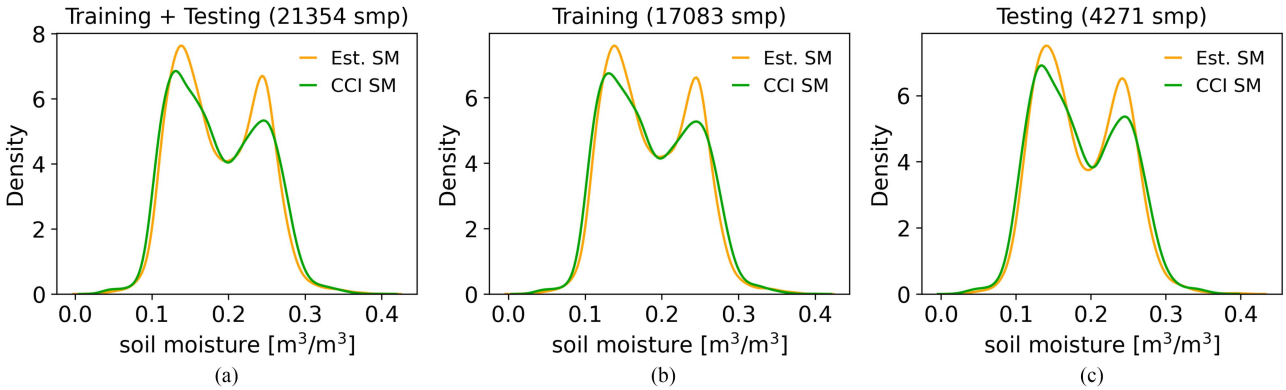

Fig. 5. Kernel density estimate of the distribution of the SM data computed for both the original ESA CCI SM (green) and the estimated SM at 0.25° (orange). They are obtained for (a) all available data, (b) SM associated with the training data, and (c) SM associated with the testing data.

D. Analysis of the Results

This section outlines the methodology employed to obtain the results presented in Section IV. It comprises three sections: the first focuses on model evaluation to ensure proper training, followed by spatial analysis techniques applied at both low and high resolutions. The final section delves into the methodology used for temporal analyses.

1) Model Evaluation: In the training phase of the model, the progression of error (RMSE), accuracy (as referred to in Section III-C1), and the explained variance are examined over successive epochs (see Fig. 4). Upon completion of training, it is ensured that the general distribution of SM samples remains consistent with the original dataset (see Fig. 5). Subsequently, the estimated SM undergoes statistical analysis in relation to the original data, employing metrics such as R^2, MAE, and RMSE for this purpose (see Fig. 6).

2) Spatial Evaluation: Continuing with the spatial evaluation at low resolution, daily SM maps corresponding to each of the five training models are derived and averaged on a daily basis to obtain at most one map per day. These computed maps undergo an error analysis, initially conducted through direct samplewise computation by subtracting the reference SM value from the estimated SM. This approach allows for an examination of the error characteristics via histogram distribution. Subsequently, the MAE is computed for every pixel within the study area, affording an investigation into the spatial distribution of errors (see Fig. 7). Furthermore, illustrative maps displaying estimated SM at low resolution are presented alongside the original ESA CCI SM maps, accompanied by the associated error, for selected days (see Fig. 8).

The trained ML model, in conjunction with the high-resolution input variables, facilitates the generation of 60-m resolution SM maps, which are computed on a daily basis. An analysis of the power density spectrum (PDS) is conducted to evaluate the effective spatial resolution of the resulting SM maps at 60 m [65] (see Fig. 9). The principal steps involved in deriving the PDS include the following.

1) Calculation of the autocovariance of the map for various spatial displacements, in steps of one pixel, conducted separately in both the zonal (longitudinal) and meridional (latitudinal) directions. All the pixel pairs with valid data in the original and in the shifted map are considered. This process is applied to both the ESA CCI SM at 0.25° and the 60-m resolution maps.
2) Computation of the Fourier transform applied to the autocovariance function, facilitating the conversion from spatial to frequency domain.

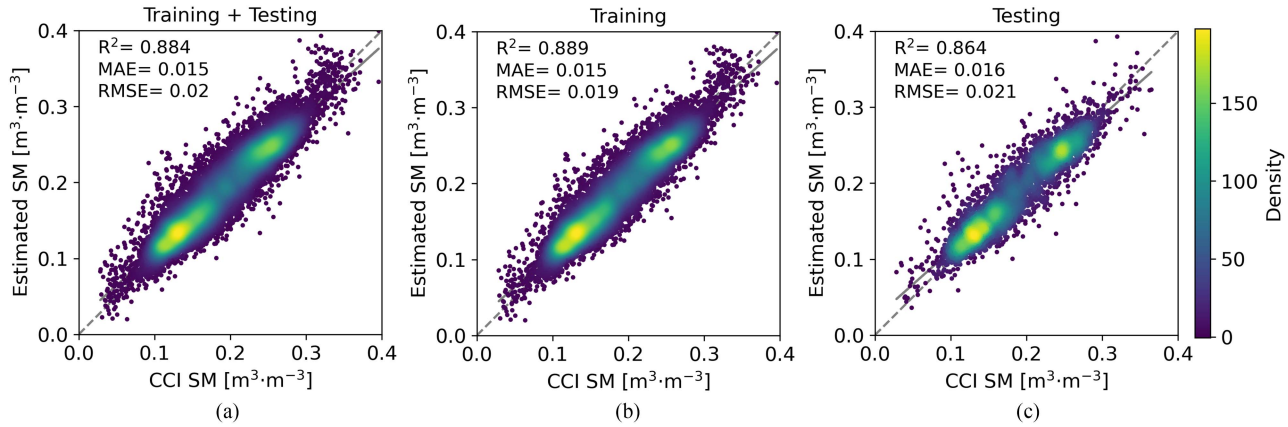

Fig. 6. Scatter plot depicting the correlation between the original ESA CCI SM dataset and the estimated SM values, employing (a) all available instances, (b) training dataset, and (c) testing dataset.

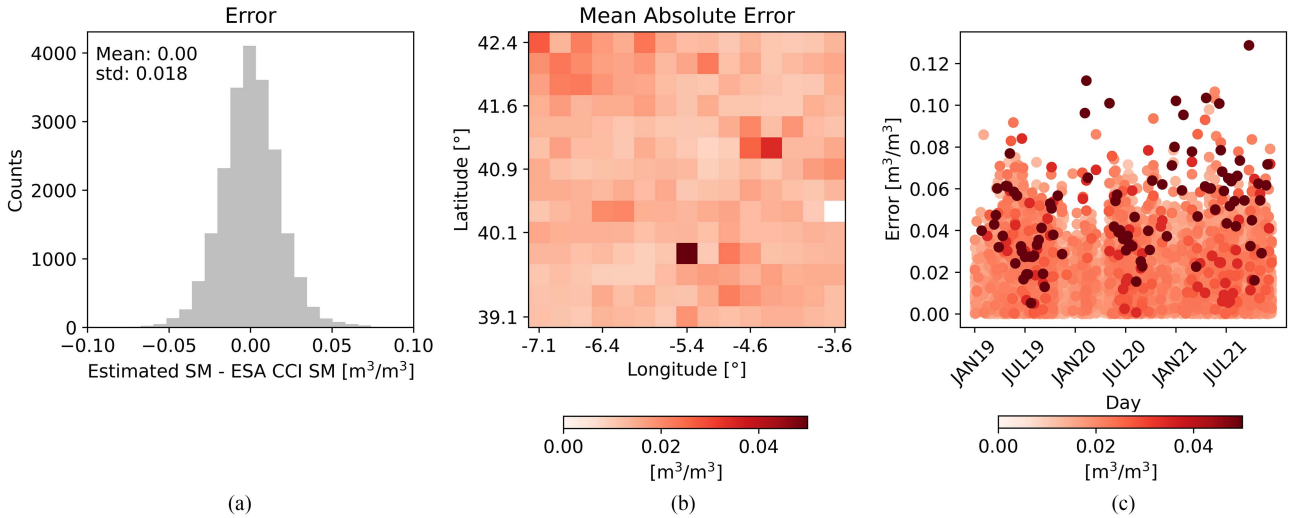

Fig. 7. Error in the estimation of SM at low resolution. (a) Histogram illustrating the distribution of the errors (estimated SM minus the original ESA CCI SM), which is centered around 0 with an std of 0.018 m^3/m^3. (b) MAE obtained per pixel, where lighter shades of red denote lower error values and darker shades indicate higher errors. (c) Temporal evolution of the absolute error, with colors also indicating the MAE for each specific pixel location.

3) Determination of power spectra, which depict the energy distribution of different spatial frequencies present in the data map. Since the spatial derivatives have been computed (as finite differences), the spectra were corrected by a factor of k-2, where k is the spatial frequency depending on the wavelength λ ($k = 1/\lambda$).

In addition, an assessment of information preservation is presented by aggregating the 60-m resolution SM maps to the original 0.25° grid on a daily basis, juxtaposed with the original ESA CCI SM maps and the estimated SM map at 0.25° (see Fig. 10). Finally, selected instances for specific days are showcased, encompassing both the original study area (spanning from 38.9 °N to 42.5 °N, and from 7.2 °W to 3.5 °W) and the REMEDHUS validation site (ranging from 41.1 °N to 41.5 °N, and from 5.5 °W to 5.1 °W), nested within the original study area and hosting in situ SM stations. Detailed enlargements of areas surrounding specific in situ stations are provided, facilitating the analysis of SM patterns at a 60-m resolution. Over these magnified regions, RGB maps are also depicted, derived from Sentinel-2 bands B2 (Blue), B3 (Green), and B4 (Red) at a 10-m resolution, helping in the identification of distinct land features or variations in terrain (see Figs. 11–14).

3) Temporal Evaluation: The measurements of the REMEDHUS SM network are employed to examine the temporal behavior of the time series derived from the original ESA CCI SM dataset, as well as the SM estimates at 0.25° and 60-m resolutions. Despite REMEDHUS providing hourly in situ measurements, a daily average is utilized to ensure consistent data availability. This daily average is computed exclusively from measurements labeled as "Good," indicating that they are obtained without encountering technical or climatic issues. An exhaustive statistical analysis of the estimated SM for all available stations within the REMEDHUS network is presented in tabular format in Section IV. In addition, an exemplary time series from three of these stations is provided (see Fig. 15). All statistical metrics utilized in the subsequent sections are summarized in Table IV.

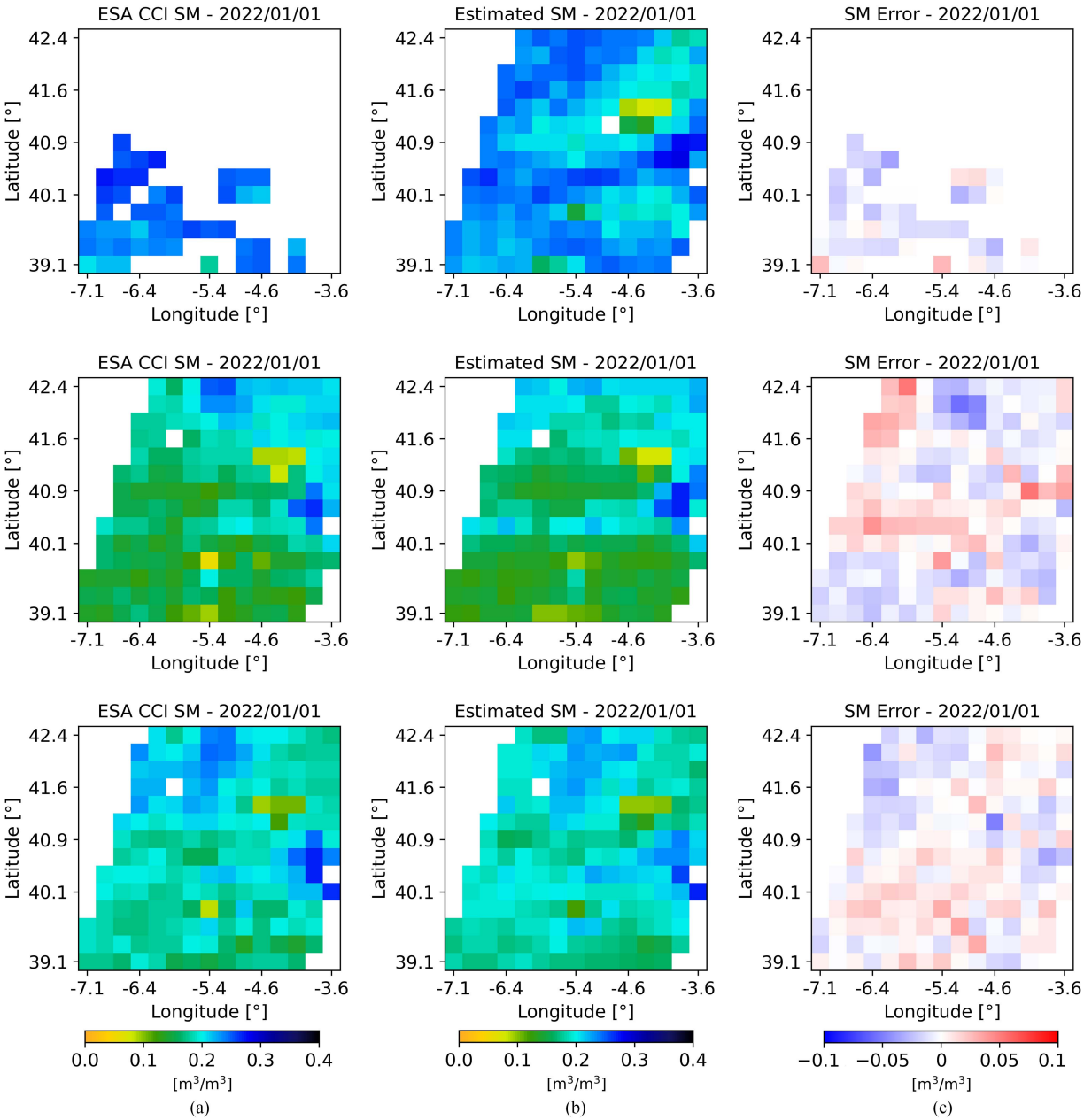

Fig. 8. (a) ESA CCI SM, (b) estimated SM at 0.25°, and (c) error maps, depicting data for 26 February 2019 (first row); 20 June 2020 (second row); and 8 October 2021 (third row).

IV. Results

The results section comprises the most pertinent findings of this research study, encompassing the performance of the ML model, as well as a spatial and temporal analysis of the estimated SM maps at 0.25° and 60-m resolution.

A. Model Evaluation

Fig. 4 depicts the evolution of losses computed using the RMSE, accuracy, and explained variance across different epochs. The blue line represents the training phase, while the orange signifies the testing phase. Although the model manages to stabilize these statistics around epoch 200, training continues for additional epochs until a significant reduction in error is no longer achieved. This stabilization occurs around epoch 800, with the RMSE plateauing at approximately 0.02 m^3/m^3, and the accuracy and the explained variance reaching a value slightly below 0.9.

Fig. 5 portrays the distribution of SM, delineating the original ESA CCI SM and the estimated SM at 0.25°. A consistent distribution is observed across the entire dataset [see Fig. 5(a)], the training dataset [see Fig. 5(b)], and the dataset allocated for testing purposes [see Fig. 5(c)]. Predominantly, samples are clustered within two ranges: one slightly below 0.15 m^3/m^3 and the other around 0.25 m^3/m^3, with a higher number of counts observed for the clusters of low values. SM values

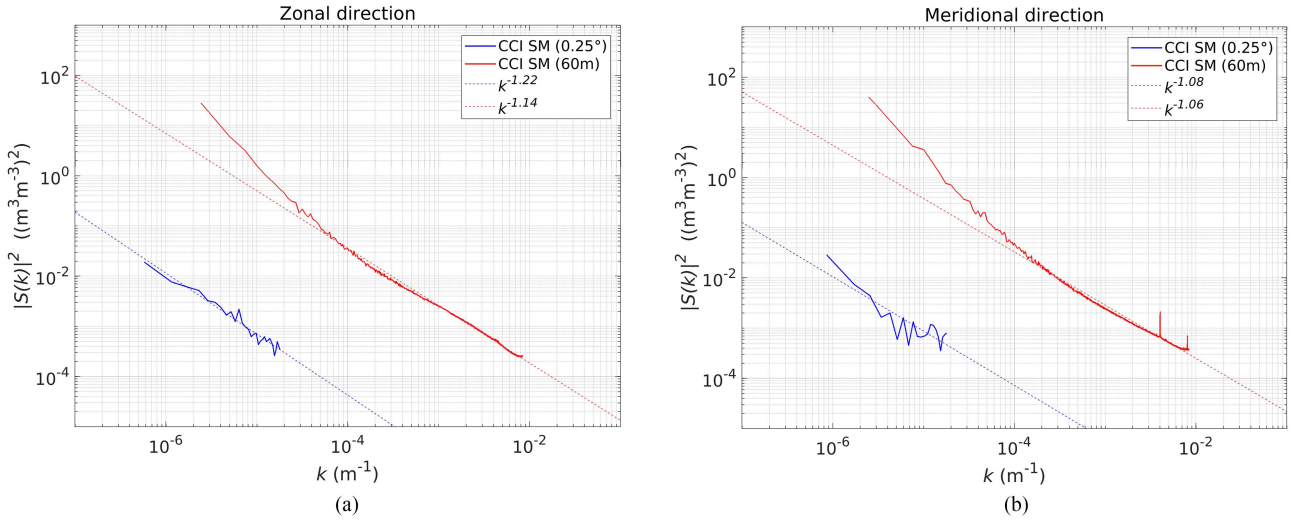

Fig. 9. Power density spectra computed for the entire study region using data derived from the ESA CCI SM maps (blue line) and the estimated SM at 60-m resolution (red line) for (a) longitudinal and (b) latitudinal directions. This analysis was conducted based on observations spanning 13 specific days in 2019: 7 January, 11 February, 28 March, 27 April, 12 May, 1 June, 1 July, 5 August, 15 August, 4 September, 9 October, 18 November, and 23 November.

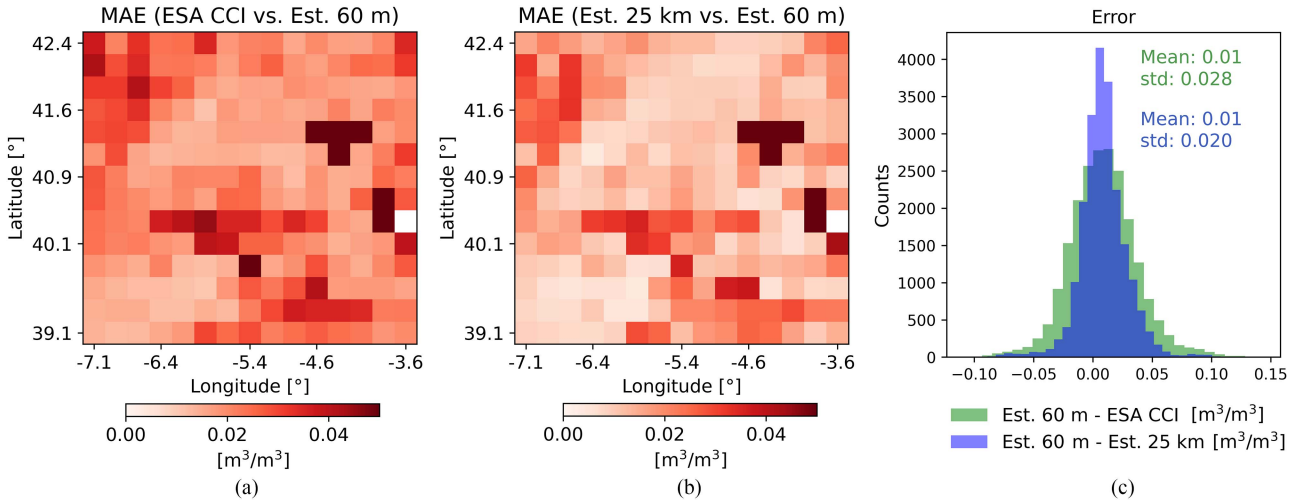

Fig. 10. Information preservation analysis. (a) MAE obtained between the aggregated 60-m resolution SM maps and the original ESA CCI SM. (b) MAE obtained between the aggregated 60-m resolution SM maps and the estimated SM at 0.25° resolution. (c) Histogram of errors.

falling below 0.1 m^3/m^3 or above 0.3 m^3/m^3 constitute 4.5% of the total dataset. This pattern is further illustrated in Fig. 6, which presents scatter plots correlating the original ESA CCI SM data with the estimated SM at low resolution, alongside relevant statistical measures, including R^2, MAE, and RMSE. In all instances, the data closely align with the 1:1 line. The statistical parameters acquired in the final epoch for the testing data encompass $R^2 = 0.86$, MAE = 0.016 m^3/m^3, and RMSE = 0.021 m^3/m^3. Notably, these metrics exhibit minimal deviation from those derived for the training data: $\Delta R^2 = 0.03$, ΔMAE = 0.001 m^3/m^3, and ΔRMSE = 0.002 m^3/m^3.

The aforementioned results correspond to Case A in Table V. This table contains the statistical outcomes for the testing dataset, resulting from training five models independently. The results are highly similar, with an R^2 of 0.86, an MAE of 0.016 m^3/m^3, and an RMSE of 0.021 m^3/m^3, on average.

B. Spatial Analysis of the Low-Resolution SM Maps

The disparity between the estimated SM values and those from the ESA CCI is portrayed via the histogram in Fig. 7(a), showcasing a Gaussian distribution centered around zero, with a std of 0.018 m^3/m^3. Fig. 7(b) displays the MAE computed per pixel over the entire study period. The distribution of errors appears largely uniform across the study region, with the exception of a specific pixel located at coordinates 39.85 °N–5.4 °W. This particular pixel corresponds to an area characterized by relatively low SM values compared to its surroundings, while maintaining similar terrain conditions. This observation is further supported by Fig. 7(c), which depicts the temporal progression of errors for each pixel within the study area. The darker marker denotes the pixel exhibiting the highest MAE value, demonstrating a consistent trend of elevated error compared to the MAE

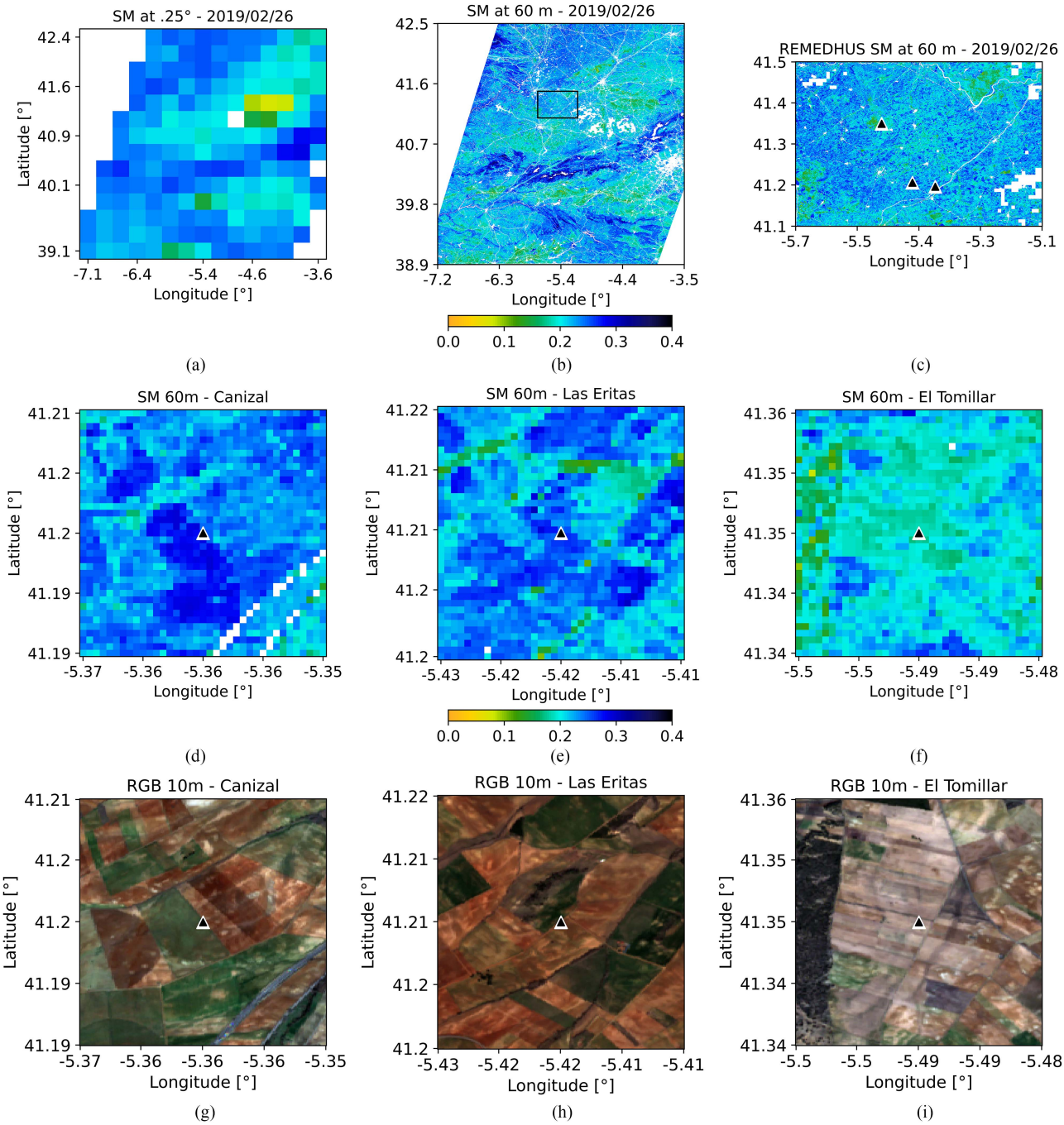

Fig. 11. Estimated SM for 26 February 2019 at resolutions of (a) 0.25° and (b) 60 m for the entire study region. The black square indicates the location of REMEDHUS. (c) Zoom of estimated SM at 60 m over the REMEDHUS area, with solid black triangles indicating the position of three in situ stations: "Cañizal," "Las Eritas," and "El Tomillar." Close-up views of the areas around these stations are depicted in (d), (e), and (f), respectively. In addition, RGB images at 10 m acquired by Sentinel-2 are shown in (g), (h), and (i), respectively.

calculated across the entire study region and period (0.015 m^3/m^3), particularly notable during the year 2021.

Fig. 8 presents a comparative analysis between the ESA CCI SM dataset [see Fig. 8(a)] and the estimated SM [see Fig. 8(b)] at a spatial resolution of 0.25° for three distinct dates, spread across varied seasons over the three-year study period: 26 February 2019 (winter); 20 June 2020 (summer); and 8 October 2021 (autumn). It is noteworthy that despite the comparatively lower sample count in the Sentinel-2 dataset as compared to the ESA CCI, owing to its revisit time or atmospheric effects, situations akin to the scenario depicted in Fig. 8 (first row) may arise, where ESA CCI SM data are largely unavailable, particularly during winter. Nonetheless, the utilization of optical data (Sentinel-2 and MODIS) facilitates the estimation of SM across nearly the entire study region. In the instance corresponding to 26 February 2019, the lower sample count results in errors slightly skewed towards negative value, with a mean error of -0.008 m^3/m^3, whereas for the remaining examples, the mean error

TABLE IV
STATISTICAL METRICS, WITH x_i AND y_i BEING THE EVALUATED SAMPLES, $\bar{x}$ AND $\bar{y}$ THE MEANS, $\hat{x}_i$ THE ESTIMATION OF x_i, AND n THE TOTAL NUMBER OF SAMPLES

Metric	Acronym	Equation	
Pearson's correlation	R	$\frac{\sum_{i=1}^{n}(x_i-\overline{x})(y_i-\overline{y})}{\sqrt{\sum_{i=1}^{n}(x_i-\overline{x})}\sqrt{\sum_{i=1}^{n}(y_i-\overline{y})}}$	(3)
Standard deviation	std	$\sqrt{\frac{1}{n}\sum_{i=1}^{n}(x_i-\overline{x})^2}$	(4)
Error	-	$\hat{x}_i - x_i$	(5)
Mean Absolute Error	MAE	$\frac{1}{n}\sum_{i=1}^{n}\lvert x_i-\hat{x}_i\rvert$	(6)
Root Mean Square Error	RMSE	$\sqrt{\frac{1}{n}\sum_{i=1}^{n}(x_i-\hat{x}_i)^2}$	(7)
Unbiased Root Mean Square Error	uRMSE	$\sqrt{\frac{1}{n}\sum_{i=1}^{n}\left((x_i-\overline{x})-(y_i-\overline{y})\right)^2}$	(8)
Bias	-	$\overline{x}-\overline{y}$	(9)
Total Variance	TV	$\frac{1}{n}\sum_{i=1}^{n}(x_i-\overline{x})^2$	(10)
Residual Variance	RV	$\frac{1}{n}\sum_{n=1}^{n}(\hat{x}_i-x_i)^2$	(11)
Explained variance	R^2	$1-\frac{RV}{TV}$	(12)

TABLE V
STATISTICAL METRICS CORRESPONDING TO THE FIVE INDEPENDENT TESTING RUNS, INCLUDING R^2, MAE, AND RMSE, COMPUTED ON THE TEST DATASET

	R^2	MAE [m^3/m^3]	RMSE [m^3/m^3]
Case A	0,864	0,016	0,021
Case B	0,858	0,016	0,022
Case C	0,869	0,016	0,021
Case D	0,866	0,016	0,021
Case E	0,863	0,016	0,021
Mean	0.864	0.016	0.021
std	0.004	0	0

approximates zero. In any case, the highest positive error recorded is 0.054 m^3/m^3, while the most negative error is -0.05 m^3/m^3.

C. Spatial Analysis of the High-Resolution SM Maps

Fig. 9 illustrates the PDS computed for the original ESA CCI SM maps (solid blue line) and the SM target maps estimated at 60 m (solid red line), separately analyzed in both the zonal [see Fig. 9(a)] and meridional [see Fig. 9(b)] directions. In addition, the fitting lines of the power spectra, represented by dashed lines, are depicted along with their respective slopes. These slopes are determined to be -1.22 for the ESA CCI and -1.14 for the 60-m SM maps in the zonal analysis and -1.08 for the ESA CCI and -1.06 for the 60-m SM maps in the meridional analysis. Notably, a discernible bias is observed between the power spectra lines corresponding to the ESA CCI and the 60-m SM maps in both analyses.

Fig. 10 depicts the MAE [see Fig. 10(a) and (b)] and the error [see Fig. 10(c)] calculated between the SM maps obtained at a 60-m resolution, aggregated to 0.25°, and the maps at low resolution, encompassing both the original ESA CCI maps and the estimated ones at 0.25° resolution. The discrepancies are slightly more pronounced when contrasting the aggregated high-resolution maps with the original ESA CCI maps than with the maps of SM estimated at 0.25°, with a mean MAE of 0.023 m^3/m^3 compared to 0.017 m^3/m^3, respectively. Spatial error patterns exhibit consistency across both comparisons. Notably, the MAE map generated when contrasting with CCI SM (characterized by higher errors) reveals three discernible patterns: 1) localized areas (4 pixels) exhibiting MAE value surpassing 0.088 m^3/m^3 (39.85 °N–5.4 °W and 41.36 °N–4.35 °W); 2) larger continuous regions (50 pixels) spanning the center, northwest, and southeast of the study area, exhibiting a mean MAE of 0.032 m^3/m^3; and 3) the remaining expanse of the study area (154 pixels) with a mean MAE of 0.018 m^3/m^3.

Upon direct comparison between the aggregated 60-m SM maps and the ESA CCI SM maps or those estimated at 0.25° [see Fig. 10(c)], the error distribution is centered around zero in both instances. Consequently, the std is marginally higher for the comparison with the ESA CCI maps (Δstd = 0.008 m^3/m^3).

The primary objective of Figs. 11–13 is to present examples of high-resolution SM maps for three distinct days spread across different seasons: 26 February 2019; 20 June 2021; and 10 October 2021. The initial depiction showcases the estimated

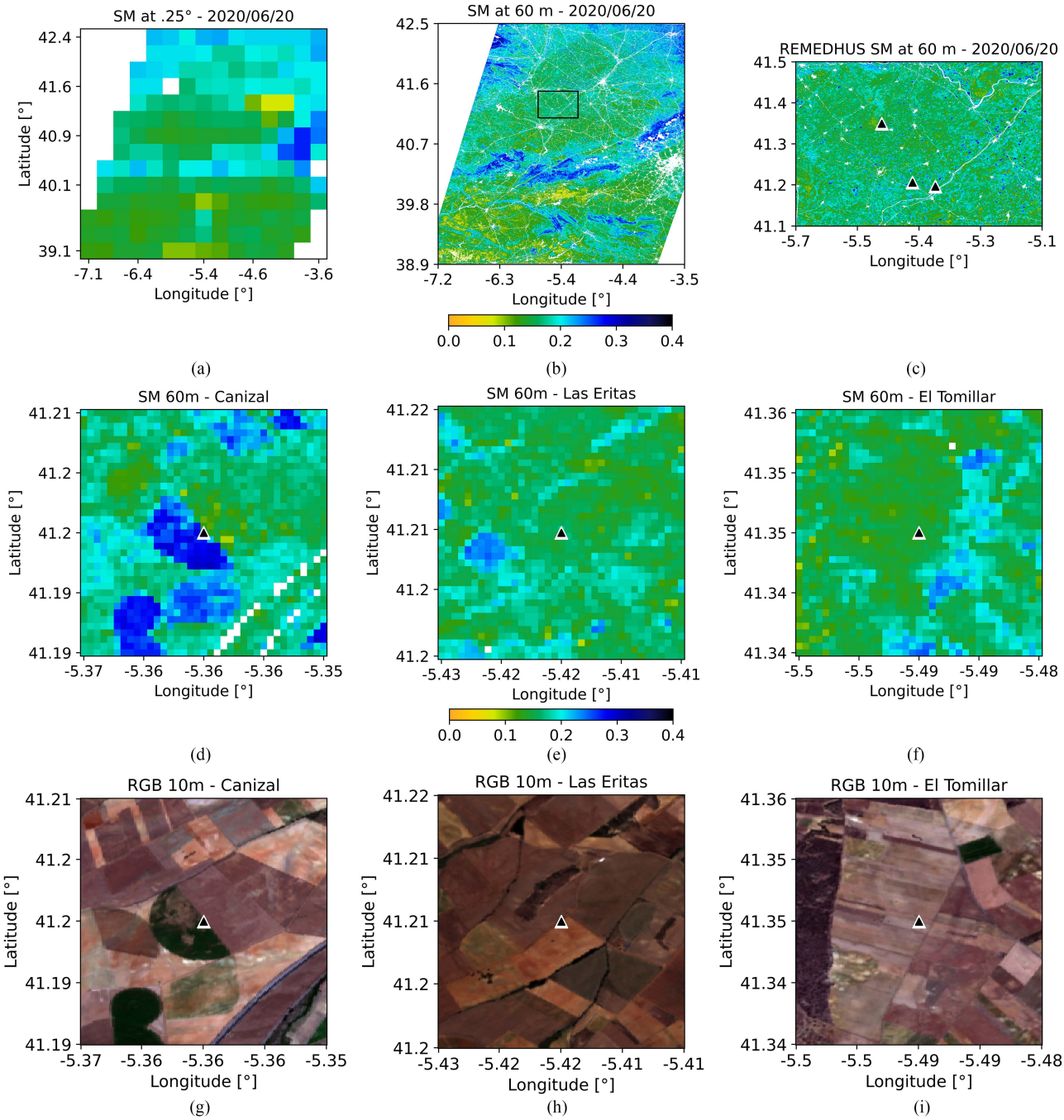

Fig. 12. Estimated SM for 20 June 2020 at resolutions of (a) 0.25° and (b) 60 m for the entire study region. The black square indicates the location of REMEDHUS. (c) Zoom of estimated SM at 60 m over the REMEDHUS area, with solid black triangles indicating the position of three in situ stations: "Cañizal," "Las Eritas," and "El Tomillar." Close-up views of the areas around these stations are depicted in (d), (e), and (f), respectively. In addition, RGB images at 10 m acquired by Sentinel-2 are shown in (g), (h), and (i), respectively.

SM at low resolution for the entire study region [see Figs. 11(a), 12(a), and 13(a)], serving as the mean SM reference level. The following images portray the SM map at 60-m resolution for the same geographical extension [see Figs. 11(b), 12(b), and 13(b)]. A subsequent examination zooms into the area that contains the REMEDHUS SM network [see Figs. 11(c), 12(c), and 13(c)], extending approximately $44 \times 50\,\text{km}^2$. Discernible spatial patterns emerge that would otherwise remain imperceptible at the 0.25° resolution of the ESA CCI SM maps. This phenomenon becomes more evident in Figs. 11–13, where the SM maps undergo further magnification to highlight exclusively three regions, each of them measuring $2.2 \times 2.2\,\text{km}^2$, corresponding to the locations of three REMEDHUS in situ stations. Spatial patterns in SM manifest certain correlations with the spatial patterns depicted in the 10-m resolution RGB maps of the same area (see Figs. 11–13). A particular evident example is elucidated in Figs. 11(d), 12(d), and 13(d), where a circular shaped field undergoes partitioning into two semicircular zones cultivated intermittently over the

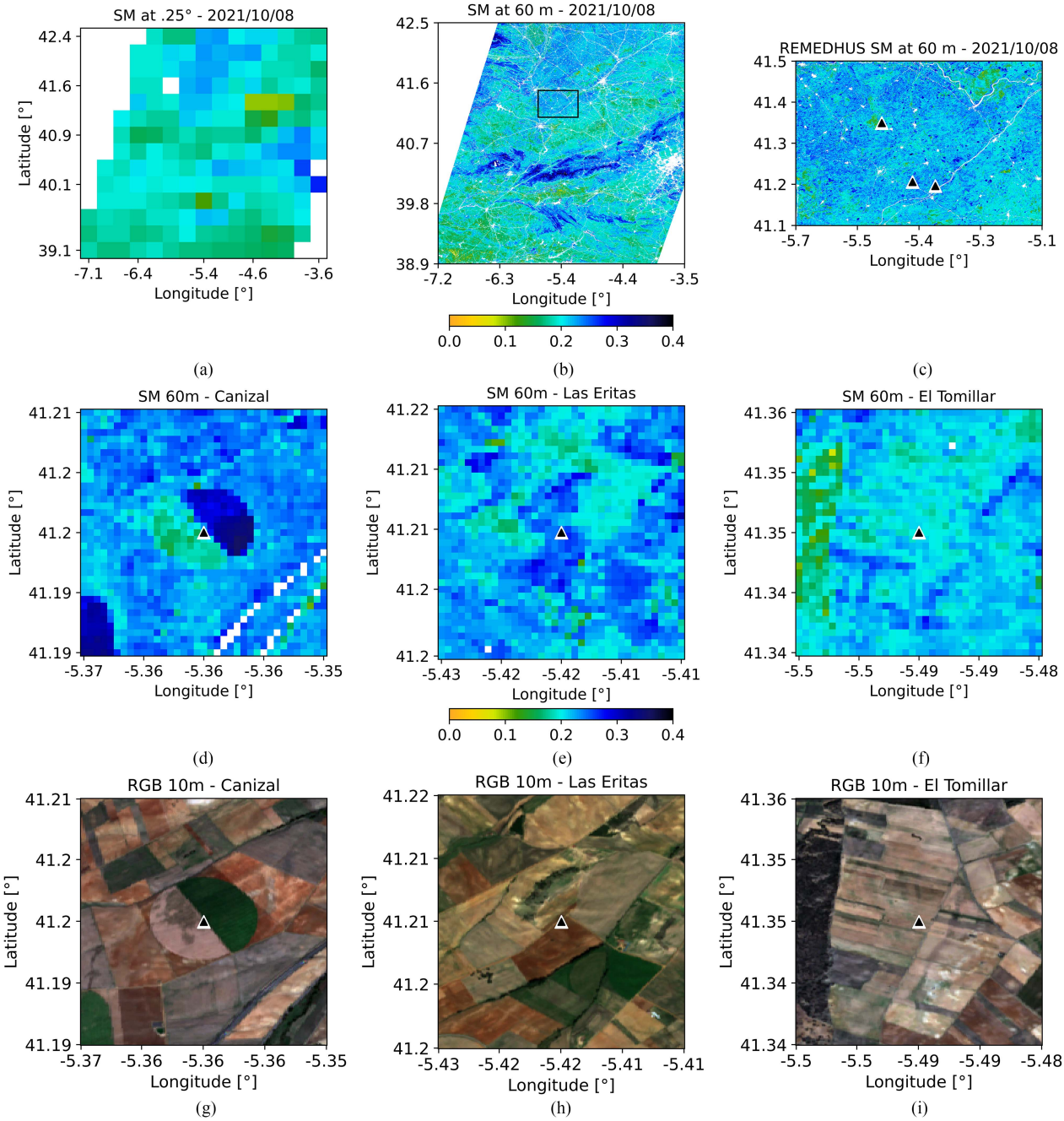

Fig. 13. Estimated SM for 10 October 2021 at resolutions of (a) 0.25° and (b) 60 m for the entire study region. The black square indicates the location of REMEDHUS. (c) Zoom of estimated SM at 60 m over the REMEDHUS area, with solid black triangles indicating the position of three in situ stations: "Cañizal," "Las Eritas," and "El Tomillar." Close-up views of the areas around these stations are depicted in (d), (e), and (f), respectively. In addition, RGB images at 10 m acquired by Sentinel-2 are shown in (g), (h), and (i), respectively.

years. This phenomenon is mirrored in the SM maps at 60-m resolution.

In Fig. 14, the average SM for each season is depicted separately for the years 2019 [see Fig. 14(a)], 2020 [see Fig. 14(b)], and 2021 [see Fig. 14(c)]. This figure facilitates the observation of SM behavior variations contingent upon geographical location and the season of the year. Certain areas consistently maintain relatively high SM values throughout the year, primarily corresponding to mountainous systems known as the "Sistema Central," "Montes de Toledo," and "Montes de León." The remaining areas demonstrate greater SM variation throughout the year, particularly in the southern half of the study region, where relatively extensive regions with the lowest SM values are observed during summer.

D. Temporal Analysis of the SM Products at High and Low Resolution

The statistical analysis, including the number of samples (N), R, bias, and uRMSE, are presented in Table VI. These

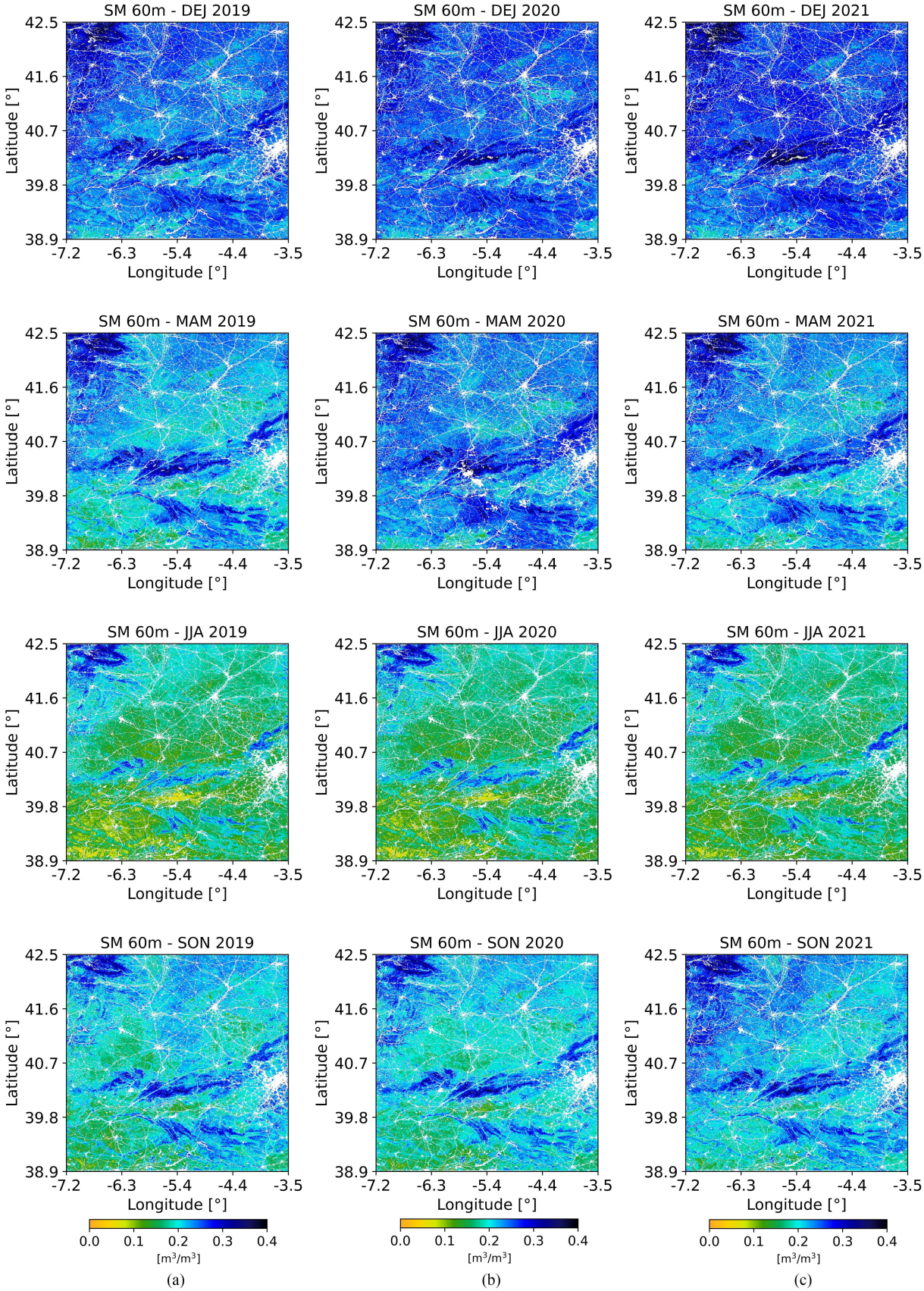

Fig. 14. Daily average of the high-resolution estimated SM maps for the following seasonal periods. (a) December, January, and February (DJF). (b) March, April, and May (MAM). (c) June, July, and August (JJA). (d) September, October, and November (SON). The columns correspond to the years 2019, 2020, and 2021.

TABLE VI
STATISTICAL COMPARISON CONDUCTED BETWEEN THE IN SITU MEASUREMENTS AND THE ESA CCI SM, AS WELL AS THE ESTIMATED SM AT 0.25° AND 60-M RESOLUTIONS

	ESA CCI 0.25° vs. in situ				Estimate 0.25° SM vs. in situ				Estimated 60-m SM vs. in situ			
Station	**N**	**R**	**Bias**	**uRMSE**	**N**	**R**	**Bias**	**uRMSE**	**N**	**R**	**Bias**	**uRMSE**
E10	921	0.78	0.161	0.041	145	0.68	0.170	**0.036**	192	0.65	0.181	**0.039**
F6	912	0.81	0.056	0.047	143	0.73	0.060	**0.045**	173	0.76	0.061	**0.045**
F11	877	0.85	0.134	0.031	82	0.81	**0.129**	**0.029**	91	0.76	**0.134**	**0.030**
H7	915	0.72	0.191	0.041	81	0.45	**0.180**	0.042	85	0.61	**0.152**	**0.035**
H9	836	0.73	−0.033	0.095	79	0.68	**−0.031**	**0.092**	90	0.72	**−0.027**	**0.088**
H13	896	0.89	0.074	0.026	75	0.86	**0.060**	0.027	87	0.83	0.101	**0.023**
I6	905	0.65	0.186	0.048	81	0.48	**0.171**	**0.042**	86	0.49	**0.160**	**0.039**
J3	852	0.68	0.191	0.042	79	0.51	**0.183**	**0.040**	87	0.62	**0.163**	**0.031**
J12	904	0.85	−0.050	0.037	77	**0.86**	−0.063	**0.034**	84	0.81	**−0.043**	0.039
K4	915	0.75	0.197	0.042	81	0.49	**0.187**	**0.041**	91	0.54	**0.188**	0.045
K9	915	0.63	0.124	0.052	81	0.45	**0.122**	0.053	85	0.59	**0.105**	**0.047**
K10	875	0.79	0.173	0.036	77	0.72	**0.164**	**0.034**	85	**0.80**	**0.150**	**0.032**
K13	902	0.57	−0.014	0.059	76	0.46	−0.032	0.063	89	**0.61**	**0.014**	**0.054**
L3	915	0.84	0.164	0.031	81	0.78	**0.156**	**0.029**	93	0.71	0.171	**0.027**
L7	877	0.59	−0.007	0.089	78	**0.59**	**−0.003**	**0.065**	83	0.54	−0.021	**0.068**
M5	906	0.79	0.099	0.035	80	0.70	**0.094**	**0.035**	90	0.71	**0.098**	0.036
M9	882	0.74	0.065	0.051	80	0.61	**0.063**	0.053	89	0.65	**0.055**	0.052
N9	885	0.64	0.032	0.061	74	0.45	**0.021**	0.073	79	0.49	0.043	0.072
O7	893	0.78	0.131	0.037	75	0.71	**0.124**	**0.033**	84	0.73	**0.126**	**0.032**

The analysis encompasses key metrics including the N, R, bias [m3/ m3], and urmse [m3/ m3] for the 19 in situ stations available during the study period. Bold values indicate higher R, lower absolute bias, and lower uRMSE compared to the original ESA CCI SM results. The gray shading indicates the stations for which their timeseries are depicted in Fig. 15.

metrics are derived from the comparison between the in situ measurements and the ESA CCI SM, and the estimated SM at different resolutions. The number of samples for the estimated SM represents approximately 10% of those available for the ESA CCI SM. The mean R has slightly decreased from 0.74 to 0.63 and 0.66 for the ESA CCI SM, the estimated SM at 0.25°, and the estimated SM at 60 m, respectively. The mean uRMSE ranges from 0.047 m^3/m^3 for the ESA CCI to 0.044 m^3/m^3 for the estimated high-resolution SM, which is close to the target error of 0.04 m^3/m^3 for the SMOS and SMAP missions. The mean absolute bias remains consistent for all three products at approximately 0.1 m^3/m^3. This temporal analysis demonstrates that high-resolution SM maps preserve virtually the same sensitivity as those from the ESA CCI.

Fig. 15 displays the time series of the in situ SM measurements alongside the ESA CCI SM, the estimated SM at 0.25°, and the estimated SM at 60 m corresponding to the three stations: "Cañizal" [see Fig. 15(a)], "Las Eritas" [see Fig. 15(b)], and "El Tomillar" [see Fig. 15(c)]. All datasets effectively capture typical seasonal trends in the study area, characterized by relatively drier conditions during springs and summers as compared to autumn and winters. While they may exhibit limitations in precisely tracking or reaching the most extreme levels of SM observed during specific events, such as the drought peaks in the spring of 2021 in "Cañizal" or the summer SM peak of 2021 in "Las Eritas," they nonetheless offer valuable insights. However, for certain stations, neither the ESA CCI SM nor the estimated SM, at either high or low resolutions, accurately captures the mean SM value.

V. DISCUSSION

A. ML Model and Low-Resolution SM Maps

The presented methodology to estimate SM has demonstrated a robust generalization to unseen data during the training phase, yielding average values (across the five trained models) of $R^2 = 0.86$, MAE = 0.016 m^3/m^3, and RMSE = 0.021 m^3/m^3. However, the ESA CCI SM exhibits a constrained dynamic range, likely due to the limitations inherent to the selected study area and period, as well as to the product itself. Consequently, a risk exists that the model may not generalize effectively beyond the study area.

Fig. 16 presents histograms of SM for ESA CCI, BEC SMOS L3 at 25 km [66] and SMAP L3 at 36 km [67], illustrating their distribution and dynamic ranges within the temporal and geographical scope analyzed in this study. The 5th and 95th percentiles stand at 0.11 m^3/m^3 and 0.3 m^3/m^3, 0 and 0.27 m^3/m^3, and 0.06 m^3/m^3 and 0.33 m^3/m^3, respectively. Notably, ESA CCI exhibits the highest mean SM value of 0.21 m^3/m^3, compared to 0.17 m^3/m^3 for SMAP and 0.10 m^3/m^3 for SMOS. It demonstrates that the dynamic range is narrower for ESA CCI, with mean SM values slightly surpassing those of SMOS and SMAP.

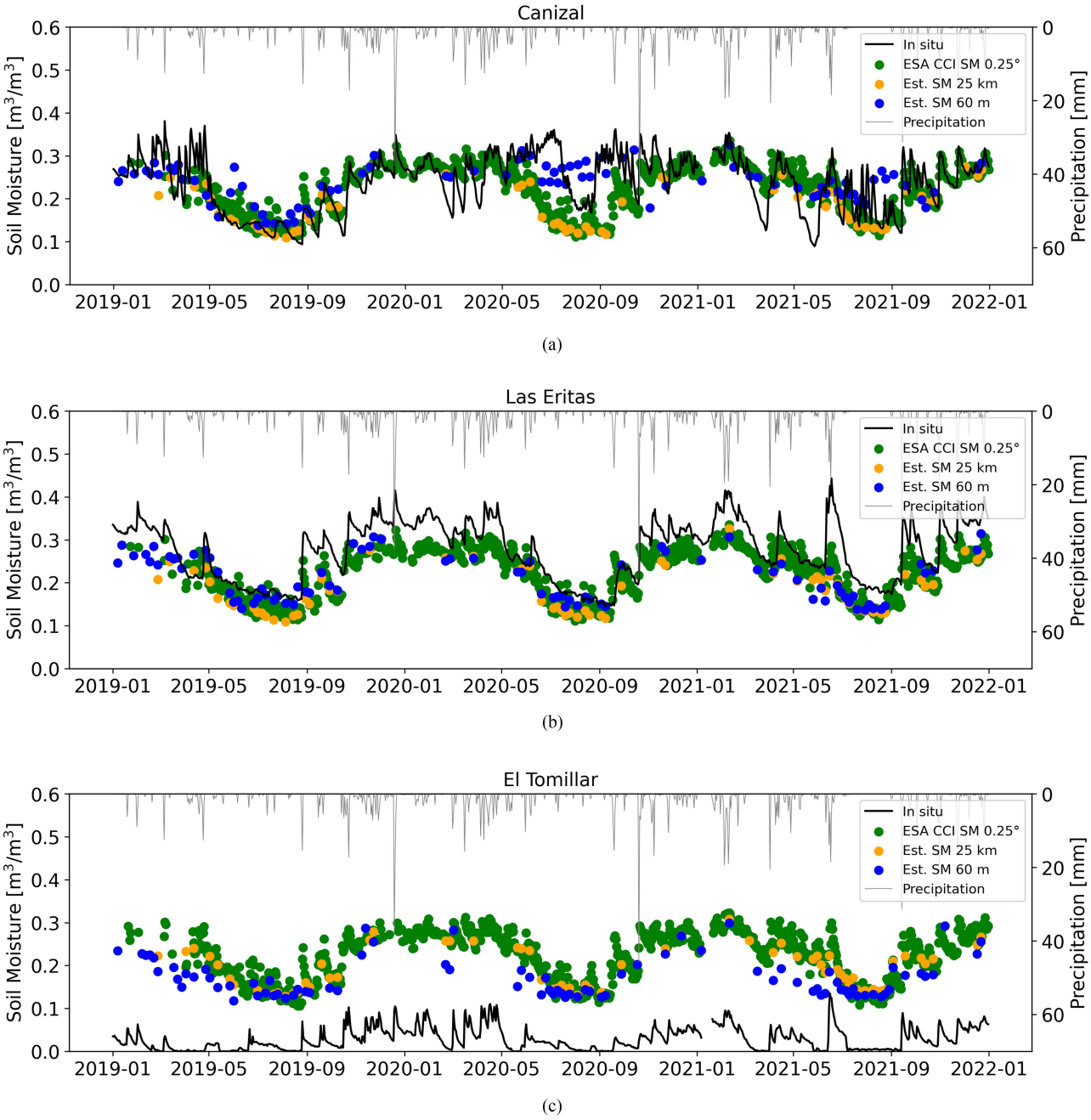

Fig. 15. Time series of the in situ SM measurements (black line), the ESA CCI SM (green dots), the estimated SM at 0.25° (orange dots), and the estimated SM at 60 m (blue dots) at three stations: (a) "Cañizal," (b) "Las Eritas," and (c) "El Tomillar." The plots also incorporate daily precipitation data (gray line).

Furthermore, the significant disparity in spatial scale between the low-resolution (0.25°) data provided by the ESA CCI and the estimated SM at high resolution (60 m) introduces potential challenges. Certain conditions at high resolution, including those related to climate, terrain, and human influence, among others, may not be captured at the lower resolution and thus may not have been fully considered during model training. As a result, there is a potential for diminished accuracy in SM estimation at higher resolutions. One possible mitigation strategy to address this challenge involves expanding the study area, thereby encompassing information that more comprehensively captures the inherent heterogeneity observed at higher resolutions.

The training process and subsequent estimation of high- and low-resolution SM maps presented in this study utilize Sentinel-2 reflectances in conjunction with spectral indices derived from them, thus incorporating information ranging from the optical range to the shortwave infrared. In addition, the process involves MODIS LST calculated from the TIR band, ERA5-Land reanalysis data, topography data (DEM and slope), and data related to soil properties (SF). Microwave sensor data, either active or passive, have not been used as predictors, as was done in previous studies [17], [30], [68], [69]. The main reason for not incorporating passive microwave data is that using predictors with very different spatial scales, such as Sentinel-2 imagery, with

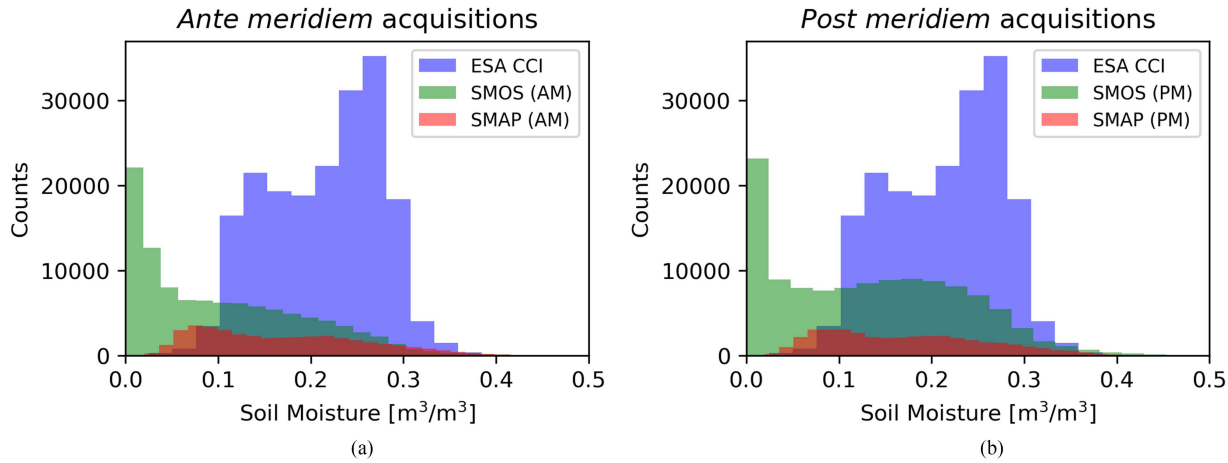

Fig. 16. Histograms of SM for ESA CCI in blue, BEC SMOS L3 at 25 km [66] in green, and SMAP L3 at 36 km [67] in red, obtained utilizing (a) *ante meridiem* acquisitions (SMOS ascending and SMAP descending orbits) and (b) *post meridiem* acquisitions (SMOS descending and SMAP ascending). All available samples during the study period have been used, resulting after applying the most restrictive quality flags for all three datasets.

resolutions ranging from 10 to 60 m depending on the band, and information from passive microwave sensors with resolutions around 40 km, can lead to a boxing effect or reduction in the effective spatial resolution of the resulting high-resolution SM maps. Moreover, the temporal desynchronization of variables must be considered. If the sensed data on a given day are intended to represent a variable on that particular day and not on another day close in time, the revisit time of the inputs is crucial for the number of available samples. For example, the difference in revisit time between Sentinel-1 (six days considering both satellites) and Sentinel-2 (five days considering both satellites) could lead to a considerable reduction in samples available for training the model, following the methodology outlined in this study. Hence, there is a mismatch that can be reflected in the performance of the high-resolution SM estimation.

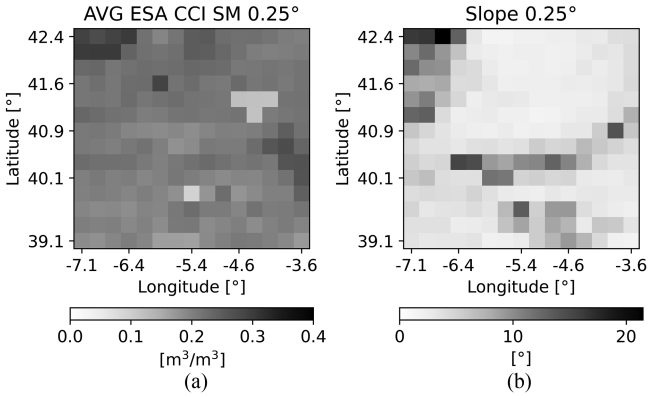

Fig. 17. (a) Average SM map for the entire study period and (b) terrain slope map, both at a resolution of 0.25°.

B. High-Resolution SM Maps: Spatial Analysis

It has been observed that high-resolution SM maps preserve the original information for most of the region (see Fig. 10). This means that when they are aggregated to low resolution and compared with the ESA CCI SM maps, the discrepancies are relatively low (with a mean MAE of 0.023 m^3/m^3). Larger differences occur in regions where the original ESA CCI maps display extreme values compared to the surrounding pixels [see Fig. 17(a)] or in areas with complicated topography or steeper slopes [see Fig. 17(b)]. This effect is clearly visible in Figs. 12(a) and (b) or in 13(a) and (b), particularly over the mountainous areas located in the northwest, denoted as the "Montes de León; the central part, identified as the "Sistema Central"; and the southern region, recognized as the "Montes de Toledo."

Validating the spatial patterns of 60-m SM maps with in situ observations is challenging due to the absence of SM networks with adequate density (i.e., with an enough number of stations homogeneously distributed over the region) to reproduce these patterns. However, high-resolution estimated SM maps (see Figs. 11–13) have been depicted alongside RGB maps (see Figs. 11–13), effectively illustrating the heterogeneity of soil coverage. Validation of high-resolution estimates is complemented by spectral analysis of the maps and by conducting time series evaluations.

In examining the spatial spectra along the zonal and meridional axes (see Fig. 9), it is observed that the slopes of the fitting lines fall within the expected range, as the PDS tends to conform to the power-law wavelength (k) such that $|S(k)|^2 \sim k^\beta$, where the slope β typically ranges between -1 and -2 [70]. At high resolution (red line in Fig. 9), the slope remains practically constant throughout the entire range of wavelengths (until $k \sim$ 8.3e-3 m-1). Since the spectrum has a positive and a negative part, the effective spatial resolution can be defined as reff $= \lambda/2 = 1/(2k)$, indicating that an effective resolution of 60 m has been achieved. The PSD might have exhibited other behaviors indicating that the desired effective resolution is not being attained. These behaviors could include the energy of the spectrum, and thus its slope, beginning to level off. This phenomenon would primarily occur in the presence of white noise, where the spectrum would behave as $|S(k)|^2 \sim k^\beta + \eta$, and consequently, for short wavelength, $|S(k)|^2$ would tend toward a constant value of η, indicating a measurement predominantly dominated by noise [65]. Alternatively, a significant drop in the PDS curve would

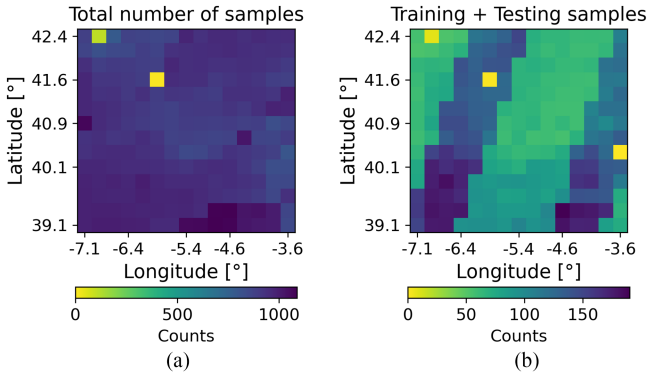

Fig. 18. (a) Total number of samples originally available for the entire study period for the ESA CCI SM, and (b) number of samples ultimately used after applying filtering based on the remaining input parameters.

suggest an effective data resolution lower than the data grid, akin to the effect of a low-pass filter at higher frequencies [71]. However, neither of these two effects is observed in Fig. 9.

Furthermore, a difference in energy is observed between the curve representing low-resolution SM maps and the one representing high-resolution maps (see Fig. 9). Enhancing the spatial resolution of the SM maps enables the assessment of finer details and structures at higher scales, thereby increasing the spatial variability within the maps. Consequently, this manifests as an increased concentration of energy within the autocovariance spectrum, leading to a higher PSD. This phenomenon explains the offset observed between the two curves.

C. High-Resolution SM Maps: Temporal Analysis

The statistical findings derived from the REMEDHUS SM network and various SM products, encompassing the ESA CCI SM, the estimated SM at 0.25°, and the estimated SM at 60 m, demonstrate significant similarities, as illustrated in Table VI. The primary distinction lies in a number of available samples for the entire study period, with 894 samples for ESA CCI, 86 for the estimated SM at 0.25°, and 97 for the estimated SM at 60 m. This decrease in the number of samples primarily arises from the five-day revisit interval of Sentinel-2 (in contrast to the one-day revisit interval for ESA CCI), leading to an approximate 89% reduction in samples across the entire study area, as depicted in Fig. 18. In addition, Table VI underscores a positive bias (SM above in situ) for both low and high-resolution estimated products, influenced by the ESA CCI SM product employed as the target for model training.

For certain REMEDHUS stations, notable differences are observed between the measurements obtained by the in situ sensors and the estimated values. This discrepancy may arise from most stations being positioned in areas where they do not interfere with agricultural activities, often at field ends or borders (refer to Figs. 11–13). Consequently, SM pixels containing these stations, even at the highest resolution, may encompass information not only from their respective fields but also from neighboring fields or pathways, potentially exhibiting significantly different SM conditions. This effect is less pronounced for time series corresponding to stations located over representative land uses within the REMEDHUS area, such as rain-fed areas [refer to Fig. 15(b)], where the likelihood of including surrounding field information altering the time series behavior is diminished, as these areas are also likely classified as rain-fed [72]. Conversely, stations situated in vineyard areas with sandy soils as "El Tomillar" [refer to Fig. 15(c)], where water filters swiftly into deeper strata, may not be entirely captured by in situ sensors at a 5-cm depth, yet remote sensing microwave data might obtain information from deeper soil layers [73].

VI. Conclusion

This study presents a multisensor FNN-based methodology for the estimation of SM at both low (0.25°) and high (60 m) resolutions. A total of 14 predictors are utilized for this purpose, including reflectances (B5, B6, B8A, and B11) and spectral indices (NDVI, EVI, GNDVI, and MSI) from Sentinel-2, LST from MODIS, precipitation from ERA5-Land, elevation and slope from SRTM, and SF from SoilGrids250m. The ESA CCI SM serves as the target variable. To estimate the high-resolution SM, a two-step methodology is employed (see Fig. 3).

1) Training at low resolution: The predictors are aggregated from their original resolution to the 0.25° grid of the target variable. The model is then trained using this information, employing an FNN designed according to the characteristics detailed in Table III.
2) Estimation at high resolution: All predictors are applied at 60 m, being interpolated to this grid size if necessary. Subsequently, they are used in conjunction with the model previously trained in the first step, ultimately facilitating the estimation of SM at a 60-m resolution.

At low resolution, it has been demonstrated that the trained model is capable of accurately estimating the ESA CCI SM, yielding average values (across the five trained models) of $R^2 = 0.86$, MAE $= 0.016$ m^3/m^3, and RMSE $= 0.021$ m^3/m^3. The error, quantified as the difference between the estimated SM at 0.25° and the ESA CCI SM, conforms to a normal distribution [see Fig. 7(a)], centered in zero with a std of 0.018 m^3/m^3. Furthermore, the distribution of the MAE remains relatively consistent across the entire study region [see Fig. 7(b)].

Validation of the spatial patterns at high resolution is complex due to the lack of sufficiently dense in situ data within the study region to allow for a comparison of the spatial distribution of SM. Nevertheless, the resulting high-resolution SM maps have demonstrated the ability to capture the spatial heterogeneity of the terrain at 60 m (see Figs. 11–13), preserving the information of the low-resolution SM for most of the region (see Fig. 10) while also adding relevant information at high resolution. The spectral analysis also confirms an effective spatial resolution of approximately 60 m for the SM maps (see Fig. 9).

Temporal analysis has revealed that the estimated SM at 60 m accurately captures seasonal SM trends but may exhibit limitations in tracking finer variations or reaching extreme levels of SM observed during specific events (see Fig. 15). In addition, the statistical results obtained from the resulting high-resolution product ($R = 0.66$, bias $= 0.095$ m^3/m^3, and

uRMSE = 0.044 m^3/m^3 on average) closely align with those obtained from the original ESA CCI product (see Table VI).

The presented methodology exhibits some limitations.

1) The model has been trained within a specific study area and time period, with ESA CCI-based SM values that mostly range between 0.1 and 0.3 m^3/m^3 (see Fig. 6). Therefore, there may be a risk that the model may not generalize well outside of this range.
2) Certain conditions that occur at high resolution—related to climate, terrain, or human influence, among others—may not be well represented within the 0.25° pixels and, thus, may not be captured at low resolution, due to not being considered during training.
3) The use of Sentinel-2 with a five-day revisit time, combined with potential atmospheric effects on optical data, limits the number of available samples (see Fig. 18). These limitations could likely be addressed by including new study areas and time periods to extend the dynamic range of ESA CCI SM values beyond the current range, incorporating additional information that more comprehensively captures the inherent heterogeneity observed at high resolution. In addition, Sentinel-2 data could be complemented with Landsat information [74] to increase the number of available samples.

The SM estimation method proposed in this research study is relevant for the development of a high-resolution SM product that can be extended beyond the lifetime of operational missions for SM estimation, such as SMOS and SMAP. These missions, initially planned with a 3-year lifespan, are currently in their 15th and 9th years, respectively. In addition, the model can be adapted to incorporate information from upcoming satellite missions, such as the Copernicus Imaging Microwave Radiometer mission. The resulting high-resolution SM maps can be relevant in a variety of applications, encompassing precision agriculture, water resource management, environmental monitoring, and the prevention and monitoring of natural disasters, among others.

Acknowledgment

The authors would like to thank the Water Resources Research Group of the University of Salamanca for their support and D. Llaveria for his advice.

References

[1] S. Arrhenius, "XXXI. On the influence of carbonic acid in the air upon the temperature of the ground," *Philos. Mag. J. Sci.*, vol. 41, no. 251, pp. 237–276, Apr. 1896, doi: 10.1080/14786449608620846.

[2] D. C. Harris, "Charles David keeling and the story of atmospheric CO_2 measurements," *Anal. Chem.*, vol. 82, no. 19, pp. 7865–7870, Oct. 2010, doi: 10.1021/ac1001492.

[3] World Meteorological Org., United Nations Environment Program, United Nations Educational, Scientific and Cultural Organization, International Council for Science, "Systematic observation requirements for satellite-based products for climate supplemental details to the satellite-based component of the implementation plan for the global observing system for climate in support of the UNFCCC," WMO Rep., Geneva, Switzerland, 2011. [Online]. Available: https://library.wmo.int/idurl/4/48411

[4] S. Bojinski, M. Verstraete, T. C. Peterson, C. Richter, A. Simmons, and M. Zemp, "The concept of essential climate variables in support of climate research, applications, and policy," *Bull. Amer. Meteorol. Soc.*, vol. 95, no. 9, pp. 1431–1443, Sep. 2014, doi: 10.1175/BAMS-D-13-00047.1.

[5] T. Schmugge, "Applications of passive microwave observations of surface soil moisture," *J. Hydrol.*, vol. 212/213, pp. 188–197, Dec. 1998, doi: 10.1016/S0022-1694(98)00209-1.

[6] Y. H. Kerr et al., "The SMOS mission: New tool for monitoring key elements of the global water cycle," *Proc. IEEE*, vol. 98, no. 5, pp. 666–687, May 2010, doi: 10.1109/JPROC.2010.2043032.

[7] D. Entekhabi et al., "The soil moisture active passive (SMAP) mission," *Proc. IEEE*, vol. 98, no. 5, pp. 704–716, May 2010, doi: 10.1109/JPROC.2010.2043918.

[8] E. Rajasekaran et al., "SMAP soil moisture change as an indicator of drought conditions," *Remote Sens.*, vol. 10, no. 5, May 2018, Art. no. 788, doi: 10.3390/rs10050788.

[9] C. Forgotson et al., "How satellite soil moisture data can help to monitor the impacts of climate change: SMAP case studies," *IEEE J. Sel. Topics Appl. Earth Observ. Remote Sens.*, vol. 13, pp. 1590–1596, 2020, doi: 10.1109/JSTARS.2020.2982608.

[10] UNESCO on behalf of UN-Water, *The United Nations World Water Development Report 2023: Partnerships and Cooperation for Water*. Paris, France: UNESCO, 2023.

[11] J. Shah et al., "Increasing footprint of climate warming on flash droughts occurrence in Europe," *Environ. Res. Lett.*, vol. 17, no. 6, Jun. 2022, Art. no. 064017, doi: 10.1088/1748-9326/ac6888.

[12] S. Sabaghy et al., "Comprehensive analysis of alternative downscaled soil moisture products," *Remote Sens. Environ.*, vol. 239, Mar. 2020, Art. no. 111586, doi: 10.1016/j.rse.2019.111586.

[13] J. Peng, A. Loew, O. Merlin, and N. E. C. Verhoest, "A review of spatial downscaling of satellite remotely sensed soil moisture," *Rev. Geophys.*, vol. 55, no. 2, pp. 341–366, Jun. 2017, doi: 10.1002/2016RG000543.

[14] N. N. Das et al., "SMAP/Sentinel-1 L2 radiometer/radar 30-second scene 3 km EASE-grid soil moisture, version 3," NASA Nat. Snow Ice Data Center Distrib. Active Arch. Center, 2020, doi: 10.5067/ASB0EQO2LYJV.

[15] O. Merlin, M. J. Escorihuela, M. A. Mayoral, O. Hagolle, A. Al Bitar, and Y. Kerr, "Self-calibrated evaporation-based disaggregation of SMOS soil moisture: An evaluation study at 3 km and 100 m resolution in Catalunya, Spain," *Remote Sens. Environ.*, vol. 130, pp. 25–38, Mar. 2013, doi: 10.1016/j.rse.2012.11.008.

[16] M. Piles et al., "A downscaling approach for SMOS land observations: Evaluation of high-resolution soil moisture maps over the Iberian Peninsula," *IEEE J. Sel. Topics Appl. Earth Observ. Remote Sens.*, vol. 7, no. 9, pp. 3845–3857, Sep. 2014, doi: 10.1109/JSTARS.2014.2325398.

[17] G. Portal et al., "A spatially consistent downscaling approach for SMOS using an adaptive moving window," *IEEE J. Sel. Top. Appl. Earth Observ. Remote Sens.*, vol. 11, no. 6, pp. 1883–1894, Jun. 2018, doi: 10.1109/JSTARS.2018.2832447.

[18] P. K. Srivastava, D. Han, M. R. Ramirez, and T. Islam, "Machine learning techniques for downscaling SMOS satellite soil moisture using MODIS land surface temperature for hydrological application," *Water Resour. Manage.*, vol. 27, no. 8, pp. 3127–3144, Jun. 2013, doi: 10.1007/s11269-013-0337-9.

[19] J. Du, J. S. Kimball, R. Bindlish, J. P. Walker, and J. D. Watts, "Local scale (3-m) soil moisture mapping using SMAP and planet SuperDove," *Remote Sens.*, vol. 14, no. 15, Aug. 2022, Art. no. 3812, doi: 10.3390/rs14153812.

[20] A. L. Samuel, "Some studies in machine learning using the game of checkers," *IBM J. Res. Develop.*, vol. 3, no. 3, pp. 210–229, Jul. 1959, doi: 10.1147/rd.33.0210.

[21] F. Rosenblatt, "The perceptron: A probabilistic model for information storage and organization in the brain," *Psychol. Rev.*, vol. 65, no. 6, pp. 386–408, 1958, doi: 10.1037/h0042519.

[22] D. P. Kingma and J. Ba, "Adam: A method for stochastic optimization," in *Proc. Int. Conf. Learn. Representations*, Dec. 2024, doi: 10.48550/ARXIV.1412.6980.

[23] S. Ioffe and C. Szegedy, "Batch normalization: Accelerating deep network training by reducing internal covariate shift," in *Proc. 32nd Int. Conf. Mach. Learn.*, 2015, pp. 448–456.

[24] S. K. Chaudhary et al., "Machine learning algorithms for soil moisture estimation using Sentinel-1: Model development and implementation," *Adv. Space Res.*, vol. 69, no. 4, pp. 1799–1812, Feb. 2022, doi: 10.1016/j.asr.2021.08.022.

[25] R. Salunke, M. Nobahar, O. E. Alzeghoul, S. Khan, I. La Cour, and F. Amini, "Near-surface soil moisture characterization in Mississippi's highway slopes using machine learning methods and UAV-captured infrared and optical images," *Remote Sens.*, vol. 15, no. 7, Mar. 2023, Art. no. 1888, doi: 10.3390/rs15071888.

[26] A. Singh and K. Gaurav, "Deep learning and data fusion to estimate surface soil moisture from multi-sensor satellite images," *Sci. Rep.*, vol. 13, no. 1, Feb. 2023, Art. no. 2251, doi: 10.1038/s41598-023-28939-9.

[27] Y. Zhang, W. Han, H. Zhang, X. Niu, and G. Shao, "Evaluating soil moisture content under maize coverage using UAV multimodal data by machine learning algorithms," *J. Hydrol.*, vol. 617, Feb. 2023, Art. no. 129086, doi: 10.1016/j.jhydrol.2023.129086.

[28] N. Vergopolan et al., "SMAP-HydroBlocks, a 30-m satellite-based soil moisture dataset for the conterminous US," *Sci. Data*, vol. 8, no. 1, Oct. 2021, Art. no. 264, doi: 10.1038/s41597-021-01050-2.

[29] J. Im, S. Park, J. Rhee, J. Baik, and M. Choi, "Downscaling of AMSR-E soil moisture with MODIS products using machine learning approaches," *Environ. Earth Sci.*, vol. 75, no. 15, Aug. 2016, Art. no. 1120, doi: 10.1007/s12665-016-5917-6.

[30] M. Xu et al., "Downscaling SMAP soil moisture using a wide & deep learning method over the continental United States," *J. Hydrol.*, vol. 609, Jun. 2022, Art. no. 127784, doi: 10.1016/j.jhydrol.2022.127784.

[31] A. Dosovitskiy et al., "An image is worth 16x16 words: Transformers for image recognition at scale," 2020, Accessed: Aug. 6, 2024. [Online]. Available: https://openreview.net/forum?id=YicbFdNTTy

[32] Y. LeCun, Y. Bengio, and G. Hinton, "Deep learning," *Nature*, vol. 521, no. 7553, pp. 436–444, May 2015, doi: 10.1038/nature14539.

[33] A. J. Arnfield, "Köppen climate classification," Accessed: Feb. 15, 2024. [Online]. Available: https://www.britannica.com/science/Koppen-climate-classification

[34] State Meteorological Agency, "Annual climatological summary 2019," Accessed: Feb. 15, 2024. [Online]. Available: https://www.aemet.es/documentos/es/serviciosclimaticos/vigilancia_clima/resumenes_climat/anuales/res_anual_clim_2019.pdf

[35] State Meteorological Agency, "Annual climatological summary 2020," Accessed: Feb. 15, 2024. [Online]. Available: https://www.aemet.es/documentos/es/serviciosclimaticos/vigilancia_clima/resumenes_climat/anuales/res_anual_clim_2020.pdf

[36] State Meteorological Agency, "Annual climatological summary 2021," Accessed: Feb. 15, 2024. [Online]. Available: https://www.aemet.es/documentos/es/serviciosclimaticos/vigilancia_clima/resumenes_climat/anuales/res_anual_clim_2021.pdf

[37] Á. González-Zamora, N. Sánchez, M. Pablos, and J. Martínez-Fernández, "CCI soil moisture assessment with SMOS soil moisture and in situ data under different environmental conditions and spatial scales in Spain," *Remote Sens. Environ.*, vol. 225, pp. 469–482, May 2019, doi: 10.1016/j.rse.2018.02.010.

[38] W. Dorigo et al., "The international soil moisture network: Serving earth system science for over a decade," *Hydrol. Earth Syst. Sci.*, vol. 25, no. 11, pp. 5749–5804, Nov. 2021, doi: 10.5194/hess-25-5749-2021.

[39] M. Drusch et al., "Sentinel-2: ESA's optical high-resolution mission for GMES operational services," *Remote Sens. Environ.*, vol. 120, pp. 25–36, May 2012, doi: 10.1016/j.rse.2011.11.026.

[40] "Sentinel-2 cloud masking with s2cloudless | Google Earth Engine," Google for Developers, Accessed: Jul. 31, 2024. [Online]. Available: https://developers.google.com/earth-engine/tutorials/community/sentinel-2-s2cloudless

[41] N. Gorelick, M. Hancher, M. Dixon, S. Ilyushchenko, D. Thau, and R. Moore, "Google Earth Engine: Planetary-scale geospatial analysis for everyone," *Remote Sens. Environ.*, vol. 202, pp. 18–27, Dec. 2017, doi: 10.1016/j.rse.2017.06.031.

[42] J. Acker et al., "Remote sensing from satellites," in *Reference Module in Earth Systems and Environmental Sciences*. Amsterdam, The Netherlands: Elsevier, 2014, Art. no. B9780124095489094409, doi: 10.1016/B978-0-12-409548-9.09440-9.

[43] C. Davidson, V. Jaganathan, A. N. Sivakumar, J. M. P. Czarnecki, and G. Chowdhary, "NDVI/NDRE prediction from standard RGB aerial imagery using deep learning," *Comput. Electron. Agriculture*, vol. 203, Dec. 2022, Art. no. 107396, doi: 10.1016/j.compag.2022.107396.

[44] A. A. Gitelson, Y. J. Kaufman, and M. N. Merzlyak, "Use of a green channel in remote sensing of global vegetation from EOS-MODIS," *Remote Sens. Environ.*, vol. 58, no. 3, pp. 289–298, Dec. 1996, doi: 10.1016/S0034-4257(96)00072-7.

[45] A. R. Huete, "A soil-adjusted vegetation index (SAVI)," *Remote Sens. Environ.*, vol. 25, no. 3, pp. 295–309, Aug. 1988, doi: 10.1016/0034-4257(88)90106-X.

[46] B. Gao, "NDWI—A normalized difference water index for remote sensing of vegetation liquid water from space," *Remote Sens. Environ.*, vol. 58, no. 3, pp. 257–266, Dec. 1996, doi: 10.1016/S0034-4257(96)00067-3.

[47] E. Huntjr and B. Rock, "Detection of changes in leaf water content using near- and middle-infrared reflectances☆," *Remote Sens. Environ.*, vol. 30, no. 1, pp. 43–54, Oct. 1989, doi: 10.1016/0034-4257(89)90046-1.

[48] B. M. Meneses, "Vegetation recovery patterns in burned areas assessed with Landsat 8 OLI imagery and environmental biophysical data," *Fire*, vol. 4, no. 4, Oct. 2021, Art. no. 76, doi: 10.3390/fire4040076.

[49] S. Diek, F. Fornallaz, M. E. Schaepman, and R. De Jong, "Barest pixel composite for agricultural areas using Landsat time series," *Remote Sens.*, vol. 9, no. 12, Dec. 2017, Art. no. 1245, doi: 10.3390/rs9121245.

[50] C. O. Justice et al., "The moderate resolution imaging spectroradiometer (MODIS): Land remote sensing for global change research," *IEEE Trans. Geosci. Remote Sens.*, vol. 36, no. 4, pp. 1228–1249, Jul. 1998, doi: 10.1109/36.701075.

[51] AppEEARS Team, "Application for extracting and exploring analysis ready samples (AppEEARS)," NASA EOSDIS Land Processes Distributed Active Archive Center (LP DAAC), USGS/Earth Resources Observation and Science, EROS Center, Sioux Falls, SD, USA, 2023.

[52] T. G. Farr et al., "The shuttle radar topography mission," *Rev. Geophys.*, vol. 45, no. 2, Jun. 2007, Art. no. 2005RG000183, doi: 10.1029/2005RG000183.

[53] Earth Resources Observation And Science (EROS) Center, "Shuttle radar topography mission (SRTM) 1 arc-second global," U.S. Geological Survey, 2017, doi: 10.5066/F7PR7TFT.

[54] W. Dorigo et al., "ESA soil moisture climate change initiative (Soil_Moisture_cci): Version 07.1 data collection," NERC EDS Centre for Environmental Data Analysis, 2023. [Online]. Available: https://catalogue.ceda.ac.uk/uuid/ea3eb0714dc6402b905fe9f7ee50dbbc/?jump=related-docs-anchor

[55] N. Tsendbazar, P. Xu, M. Herold, M. Lesiv, and M. Duerauer, "WorldCover product validation report (version 2.0)," *Eur. Space Agency*, Mar. 2022. [Online]. Available: https://worldcover2021.esa.int/data/docs/WorldCover_PVR_V2.0.pdf

[56] T. Hengl et al., "SoilGrids250m: Global gridded soil information based on machine learning," *PLoS One*, vol. 12, no. 2, Feb. 2017, Art. no. e0169748, doi: 10.1371/journal.pone.0169748.

[57] T. Hengl, "Clay content in % (kg /kg) at 6 standard depths (0, 10, 30, 60, 100 and 200 cm) at 250 m resolution," *Zenodo*, Nov. 2018, doi: 10.5281/ZENODO.2525663.

[58] T. Hengl, "Sand content in % (kg /kg) at 6 standard depths (0, 10, 30, 60, 100 and 200 cm) at 250 m resolution," *Zenodo*, Dec. 2018, doi: 10.5281/ZENODO.2525662.

[59] J. Muñoz-Sabater et al., "ERA5-Land: A state-of-the-art global reanalysis dataset for land applications," *Earth Syst. Sci. Data*, vol. 13, no. 9, pp. 4349–4383, Sep. 2021, doi: 10.5194/essd-13-4349-2021.

[60] "scipy.interpolate.griddata—SciPy v1.12.0 Manual," Accessed: Feb. 19, 2024. [Online]. Available: https://docs.scipy.org/doc/scipy/reference/generated/scipy.interpolate.griddata.html

[61] W. Kirch, Ed., "z-Score," in *Encyclopedia of Public Health*. Berlin, Germany: Springer-Verlag, 2008, pp. 1484–1484, doi: 10.1007/978-1-4020-5614-7_3826.

[62] S. S. Haykin and S. S. Haykin, *Neural Networks and Learning Machines*, 3rd ed. Englewood Cliffs, NJ, USA: Prentice-Hall, 2009.

[63] A. Paszke et al., "PyTorch: An imperative style, high-performance deep learning library," in *Proc. 33rd Int. Conf. Neural Inf. Process. Syst.*, 2019, pp. 8026–8037.

[64] F. Pedregosa et al., "Scikit-learn: Machine learning in python," *J. Mach. Learn. Res.*, vol. 12, pp. 2825–2830, Nov. 2011.

[65] N. Hoareau, A. Turiel, M. Portabella, J. Ballabrera-Poy, and J. Vogelzang, "Singularity power spectra: A method to assess geophysical consistency of gridded products—Application to sea-surface salinity remote sensing maps," *IEEE Trans. Geosci. Remote Sens.*, vol. 56, no. 9, pp. 5525–5536, Sep. 2018, doi: 10.1109/TGRS.2018.2819240.

[66] M. Pablos, C. González-Haro, M. Piles, and G. Portal, "BEC SMOS soil moisture products description," Barcelona Expert Center, Barcelona, Spain, Oct. 2022. [Online]. Available: http://hdl.handle.net/10261/303808

[67] P. E. ONeill, S. Chan, E. G. Njoku, T. Jackson, and R. Bindlish, "SMAP L3 radiometer global daily 36 km EASE-grid soil moisture, version 6," 2019. [Online]. Available: https://nsidc.org/data/spl3smp/versions/6

[68] N. N. Das et al., "The SMAP and Copernicus Sentinel 1A/B microwave active-passive high resolution surface soil moisture product," *Remote Sens. Environ.*, vol. 233, Nov. 2019, Art. no. 111380, doi: 10.1016/j.rse.2019.111380.

[69] G. Portal et al., "Impact of incidence angle diversity on SMOS and Sentinel-1 soil moisture retrievals at coarse and fine scales," *IEEE Trans. Geosci. Remote Sens.*, vol. 60, 2022, Art. no. 4412218, doi: 10.1109/TGRS.2022.3187467.

[70] A. Turiel, J. Solé, V. Nieves, J. Ballabrera-Poy, and E. García-Ladona, "Tracking oceanic currents by singularity analysis of microwave sea surface temperature images," *Remote Sens. Environ.*, vol. 112, no. 5, pp. 2246–2260, May 2008, doi: 10.1016/j.rse.2007.10.007.
[71] V. González-Gambau et al., "Triple collocation analysis for two error-correlated datasets: Application to L-band brightness temperatures over land," *Remote Sens.*, vol. 12, no. 20, Oct. 2020, Art. no. 3381, doi: 10.3390/rs12203381.
[72] G. Portal et al., "Assessment of multi-scale SMOS and SMAP soil moisture products across the Iberian Peninsula," *Remote Sens.*, vol. 12, no. 3, Jan. 2020, Art. no. 570, doi: 10.3390/rs12030570.
[73] F. T. Ulaby and D. G. Long, *Microwave Radar and Radiometric Remote Sensing*. Ann Arbor, MI, USA: Univ. Michigan Press, 2014.
[74] M. Claverie et al., "The harmonized Landsat and Sentinel-2 surface reflectance data set," *Remote Sens. Environ.*, vol. 219, pp. 145–161, Dec. 2018, doi: 10.1016/j.rse.2018.09.002.

Gerard Portal (Member, IEEE) was born in Barcelona, Spain, in 1988. He received the degree in telecommunication engineering in 2015 and the Ph.D. degree in signal theory and communications in 2022, both from the Polytechnic University of Catalonia (UPC), Barcelona.

In 2016, he joined the Department of Signal Theory and Communications, UPC, as a Senior Research Support Technician. Since 2021, he has been working as a Technical Engineer with the Institute of Space Studies of Catalonia, Barcelona. He has contributed to the development and enhancement of soil moisture disaggregation algorithms and has been involved in the analysis of passive and active microwave parameters. His research interests include both active and passive remote sensing, as well as the development of downscaling algorithms by leveraging synergies from data acquired by different sensors (optical, thermal, and at microwave frequencies).

Mercè Vall-Llossera (Senior Member, IEEE) was born in Lleida, Spain. She received the Telecommunications Engineer and Ph.D. degrees in telecommunications engineering from the Universitat Politècnica de Catalunya (UPC), Barcelona, Spain, in 1990 and 1994, respectively.

Since 1990, she has been teaching with Escuela Técnica Superior de Ingeniería de Telecomunicaciones de Barcelona, UPC. During the Ph.D., she was working on numerical methods applied to radar target characterization and antenna design. She applied high-frequency approximations to radar analysis and graphical processing for parabolic antenna design. Since 1998, her research has been devoted to passive remote sensing, working in the Earth Explorer mission (European Spatial Agency (ESA) Soil Moisture and Ocean Salinity (SMOS) with the Passive RSLab team within the frame of several contracts with the ESA), directly or as subcontractors of some enterprises (EADS-Casa Espacio, Deimos Engiheria). Her research experience involves interferometric radiometry, SMOS retrieval, downscaling algorithm for spatial resolution improvement, and added-value products from SMOS, AQUARIUS, and soil moisture active passive missions. Nowadays, she is interested in L-band soil moisture and VOD new applications, such as drought detection, pest and plague monitoring, crop yield and biomass estimations, and forest fire prevention.

Dr. Vall-llossera was a recipient of the first prize of the European Information and Technology Prize in 1998. She is a Regular Reviewer of IEEE TRANSACTIONS ON GEOSCIENCE AND REMOTE SENSING, *Journal of Hydrology*, *Remote Sensing of Environment*, IEEE JOURNAL OF SELECTED TOPICS IN APPLIED EARTH OBSERVATIONS AND REMOTE SENSING, IEEE GEOSCIENCE AND REMOTE SENSING LETTERS, International Geoscience and Remote Sensing Symposium (IGARSS), *Journal of Earth System Science*, *Journal of Hydrometeorology*, and *Water Resources Research*. In 2007, she participated in the organization of IGARSS.

Carlos López-Martínez (Senior Member, IEEE) received the M.Sc. degree in electrical engineering and the Ph.D. degree in remote sensing from the Universitat Politècnica de Catalunya (UPC), Barcelona, Spain, in 1999 and 2003, respectively, and the Postgraduate Diploma degree in data science and Big Data from the Universitat de Barcelona, Barcelona, in 2021.

He is currently an Associate Professor in the area of remote sensing and microwave technology with UPC. He has a large professional international experience with the German Aerospace Center (DLR), Germany, with the University of Rennes 1, Rennes, France, and as the Group Leader of the Remote Sensing and Natural Resources Modeling Team, Luxembourg Institute of Science and Technology, Esch-sur-Alzette, Luxembourg. He has broad academic teaching experience from bachelor's, master's, and Ph.D. levels to advanced technical tutorials presented at international conferences and space and research institutions worldwide. He has authored more than 200 articles in journals, books, and conference proceedings. His research interests include synthetic aperture radar (SAR) theory, statistics and applications, multidimensional SAR, radar polarimetry, physical parameter inversion, advanced digital signal processing, estimation theory, and harmonic analysis.

Dr. López-Martínez was a recipient of the EUSAR 2002 Conference Student Prize Paper Award, the EUSAR 2012 Conference First Place Student Paper Award, as a coauthor, and the IEEE-GRSS 2013 GOLD Early Career Award. He has collaborated with the Spanish PAZ and the European Spatial Agency's (ESA) SAOCOM-CS missions and in the proposal of the Parsifal mission. He is a member of the ESA's Sentinel ROSE-L Mission Advisory Group. He was appointed the Vice President of the IEEE-GRSS Spanish Chapter, and in 2016, he became a Secretary and a Treasurer. Since 2011, he has been collaborating with the IEEE-GRSS Globalization initiative in Latin America, contributing to the creation of the IEEE-GRSS Chilean Chapter and the organization of the 2020 LAGIRSS conference, being appointed as Latin America Liaison in 2019. He is also the Co-Chair of the Tutorial Technical Committee of the Indian 2020 and 2021 InGARSS conferences. He is an Associate Editor for IEEE JOURNAL OF SELECTED TOPICS IN APPLIED EARTH OBSERVATIONS AND REMOTE SENSING and *Remote Sensing* (MDPI), acting also as an invited Guest Editor for several special issues.

Adriano Camps (Fellow, IEEE) joined the Electromagnetics and Photonics Engineering Group, Department of Signal Theory and Communications, Universitat Politècnica de Catalunya (UPC), Barcelona, Spain, as an Assistant Professor, in 1993, an Associate Professor in 1997, and has been a Full Professor since 2007. In 1999, he was on sabbatical leave with the Microwave Remote Sensing Laboratory, University of Massachusetts at Amherst, Amherst, MA, USA. He has authored or coauthored more than 269 articles published in peer-reviewed journals, nine book chapters, and the book with Emery *Introduction to Satellite Remote Sensing: Atmosphere, Ocean, Land and Cryosphere Applications* (Elsevier, 2017), and more than 542 conference presentations. His H-index is 64/51, and his publications have received more than 16.518/11.531 citations, and has advised 31 Ph.D. thesis students (more than eight on-going) and more than 160 final projects and M.Eng. theses.

Dr. Camps was the recipient of several awards, including the European Young Investigator Award in 2004, the Catalan Institution for Research and Advanced Studies (ICREA) Academia Research Award in 2009 and 2015, the Duran Farell Award for Technology Transfer in 2000, 2010, and 2022, and the 2021 IEEE GRSS Education Award.

Miriam Pablos (Member, IEEE) received the B.Sc. degree in telecommunications engineering and the Ph.D. degree in signal theory and communications from the Universitat Politècnica de Catalunya (UPC), Barcelona, Spain, in 2010 and 2016, respectively.

In 2009, she joined the Department of Signal Theory and Communications, UPC, as a Research Fellow. From January to April 2011, she was with the Institute of Space Studies of Catalonia (IEEC). She developed her Ph.D. thesis from 2011 to 2016, in collaboration with the Barcelona Expert Center (BEC) on Remote Sensing. She was a Visiting Ph.D. Student with the Department of Civil and Environmental Engineering, Massachusetts Institute of Technology (MIT), Cambridge, MA, USA, from April to June 2015. From 2017 to 2018, she was a Postdoctoral Researcher with the Instituto Hispanoluso de Investigaciones Agrarias, University of Salamanca (USAL), Villamayor, Spain. In 2018, she became a Member of the BEC again. From 2018 to 2021, she was with the Spanish National Research Council (CSIC). From September to December 2021, she was a Project Assistant with the Technical University of Vienna (TU-Wien), Vienna, Austria. From May to August 2022, she was with CSIC. Since October 2022, she has been a Postdoctoral Researcher with UPC. She collaborated with the SMOS and the Federated Satellite Systems 3Cat (FSSCat) missions. She is currently collaborating with the Copernicus Imaging Microwave Radiometer (CIMR) mission. She has currently authored 24 international journal articles and more than 35 conference proceedings. Her research interests include microwave radiometry at L-band with the Soil Moisture and Ocean Salinity (SMOS), Aquarius and Soil Moisture Active Passive (SMAP) missions, including both Level 1 (brightness temperature) and Levels 2, 3, and 4 (soil moisture), the improvement of soil moisture disaggregation algorithms from the synergy of microwave and optical (visible and infrared) data, soil moisture retrieval and disaggregation algorithms, validation of satellite soil moisture products, and development of added-value products and applications.

Alberto Alonso-González (Member, IEEE) received the B.Sc. degree in computer science, the M.Sc. degree in telecommunication engineering, and the Ph.D. degree from the Technical University of Catalonia (UPC), Barcelona, Spain, in 2007, 2009, and 2014, respectively.

From 2009 to 2014, he was with the Department of Signal Theory and Communications, UPC. From 2014 to 2022, he was with the Microwaves and Radar Institute, German Aerospace Center (DLR), Wessling, Germany, as a member of the Polarimetric SAR Interferometry Research Group. Since 2022, he has been with the CommSensLab Group, Department of Signal Theory and Communications, UPC. His research interests include multidimensional synthetic aperture radar (SAR), SAR polarimetry and interferometry, and digital signal and image processing. His research activities are focused on remote sensing data modeling and machine learning techniques applied to agricultural and forest monitoring for climate change mitigation.

Dr. Alonso-González was a recipient of the First Place Student Paper Award at the EUSAR 2012 Conference and the Extraordinary Doctoral Thesis Award from the Technical University of Catalonia in 2016.

Thomas Jagdhuber (Senior Member, IEEE) received the Diploma degree in physical geography, physics, remote sensing, and geoinformatics from the Ludwig Maximilian University of Munich, Munich, Germany, and the Technical University of Munich, Munich, in 2006, and the Ph.D. degree in hydrology from the Faculty of Science, University of Potsdam, Potsdam, Germany, in 2012.

Since 2007, he has been with the Microwaves and Radar Institute (HR), German Aerospace Center (DLR), Weßling, Germany, and since 2022, he has been leading the signatures research group of HR. From 2014 to 2019 and 2022 to 2023, he was a Yearly Visiting Scientist with the Massachusetts Institute of Technology, Boston, MA, USA, contributing to the preparation and continuation of the soil moisture active passive (SMAP) and SMAP/Sentinel-1 missions. He is also a Lecturer with the University of Jena, Jena, Germany, and a habilitation candidate with the University of Augsburg, Augsburg, Germany. His main research interests include physics-based multisensor data integration with a focus on active and passive microwave interaction theory and polarimetric techniques for hydrological, agricultural, ecological, and cryospheric parameter modeling and estimation.

Dr. Jagdhuber was a recipient of the DLR Science Award for his research on polarimetric SAR decomposition techniques in 2014. Together with Prof. Entekhabi (MIT), he was awarded the MIT-MISTI Grant for global water cycle and environmental monitoring using active and passive satellite-based microwave instruments. He also serves as a reviewer for several international journals and conference boards.

Amir Mustofa Irawan (Member, IEEE) was born in Madiun, Indonesia, in 1990. He received the master's degree in environment and climate change from the University of Liverpool, Liverpool, U.K., in 2016, funded by the Indonesia Endowment Fund for Education Scholarship. He is currently working toward the doctoral degree, supported by a fellowship from the "la Caixa" Foundation, with the Technical University of Catalonia, Barcelona, Spain, where his research focuses on the application of artificial intelligence to geoscience and remote sensing, specifically developing applications related to the effects of climate change.

Since 2010, he has been with the Indonesian Agency for Meteorology, Climatology, and Geophysics, and since 2017, he has been a Lecturer with the Department of Climatology, School of Meteorology, Climatology, and Geophysics, Jakarta, Indonesia.